Revision 3

A high resolution powder neutron diffraction study of the crystal structure of neighborite ($NaMgF_3$) between 9 K and 440 K

Kevin S. Knight[1,2,*]

[1] ISIS Facility, STFC Rutherford Appleton Laboratory, Harwell Oxford, Didcot, Oxon. OX11 0QX, UK

[2] Department of Earth Sciences, The Natural History Museum, Cromwell Road, London SW7 5BD, UK

* E-mail: kevin.knight@stfc.ac.uk

ABSTRACT

The temperature-dependence of the unit cell dimensions and the crystal structures of the fluorperovskite neighborite, $NaMgF_3$ (analysed in the *Pbnm* setting of the space group), have been determined at eighty-eight temperatures between 9 K and 440 K from high resolution, time-of-flight, powder neutron diffraction data. Lattice parameters exhibit saturation at low temperatures, before developing linear thermal expansion coefficients at temperatures above ~350 K. The temperature-dependence of each axis has been analysed, and fitted, using a two-term expression related to an Einstein internal energy function. The unit cell parameters *a*, and *c*, behave in a conventional manner, however, an unexpected, and previously unobserved, region of negative linear thermal expansion has been found for the *b* axis in the temperature interval 20 K $\leq$ T $\leq$ 90 K. Estimated, high temperature axial thermal expansion coefficients derived from the lattice parameter fitting are in good agreement with those experimentally determined from an earlier synchrotron study, and indicate that high temperature saturation has been achieved in neighborite by 440 K. The unit cell volume varies smoothly and monotonically over the whole temperature interval, and the two-term

Debye model of Barron has been successfully used to fit these data with characteristic temperatures of 369(2) K, and 1055(14) K. For the temperature interval 313.15 K – 443.15 K, the thermodynamic Grüneisen constant has been determined using the Debye parameterization of the unit cell volume, coupled with literature values of the isobaric molar heat capacity. The evolution of the crystal structure as a function of temperature is presented, and explained, in terms of the temperature-dependence of the amplitudes of the seven symmetry-adapted basis-vectors of the aristotype phase that are consistent with the orthorhombic space group. The calculated temperature variations of the bond lengths are in excellent agreement with those experimentally determined. The primary order parameters for centrosymmetric, zone-boundary phase transitions in perovskite-structured compounds, i.e. the amplitudes of the basis vectors that transform as the irreducible representations R_4^+ (anti-phase tilt), and M_3^+ (in-phase tilt), have been fitted to a Landau free energy expansion that incorporates low temperature saturation. Within the temperature range studied, the temperature dependence of the displacement corresponding to the anti-phase tilt is consistent with tricritical behavior. Experimental evidence is presented for a quadratic coupling of the in-phase tilt to the anti-phase tilt for temperatures greater than ~135 K, suggesting critical behaviour at the orthorhombic – cubic transition is purely related to an instability at the R point of the pseudocubic Brillouin zone.

Keywords: Neighborite, Rietveld refinement, crystal structure, neutron diffraction.

INTRODUCTION

For over thirty years, the thermoelastic, physical, and structural properties of the fluoroperovskite mineral neighborite (Chao et al. 1961), $NaMgF_3$, has been used as an

isostructural, isoelectronic, easily synthesised stable phase to provide experimental insight into the potential behaviour of mantle $MgSiO_3$ perovskite (O'Keeffe et al. 1979; O'Keeffe and Bovin 1979; Cheeseman and Angell 1981; Anderson et al. 1985; Zhao et al. 1993a,b, 1994a,b; Umemoto et al. 2006). In the original mineralogical description of neighborite (Chao et al. 1961), the space group setting *Pcmn* of *Pnma* was chosen by analogy with earlier work carried out on $CaTiO_3$ perovskite (Kay and Bailey, 1957). Subsequent crystallographic investigations of neighborite have settled on the alternative setting of the space group *Pnma*, space group *Pbnm* (Zhao et al. 1993a,b, 1994a,b; Mitchell et al. 2007), and it is this setting which we use in the work to be described in detail below.

Experimental investigations of neighborite have included the determination of the elastic moduli (Zhao and Weidner 1993), the temperature-dependence of the isobaric heat capacity above room temperature (Topor et al. 1997), and the equation of state (Liu et al. 2005; Martin et al. 2006). Contradictory experimental results were found for the presence of superionic conductivity in neighborite at high temperatures (O'Keeffe and Bovin 1979; Anderson et al. 1985) which remain to be resolved. The crystal structure of neighborite has been determined at high temperatures (Zhao et al. 1993a,b), at low temperatures (Mitchell et al. 2007), and at high pressures (Zhao et al. 1994a,b; Liu et al. 2005).

Detailed high temperature powder X-ray diffraction studies by Chao et al. (1961) has shown neighborite to undergo at least one structural phase transition from the ambient temperature orthorhombic hettotype phase to the cubic aristotype phase at ~1173(25) K, with a tetragonal, or pseudotetragonal phase, apparently existing between 1033 K and 1173 K. The crystal structure of neighborite between 293 K and 1173 K was subsequently investigated by Zhao et al. (1993a) using Rietveld refinement of laboratory, and higher resolution synchrotron powder X-ray diffraction data, with no evidence being found for the intermediate tetragonal phase proposed by Chao et al. (1961). At the resolution of the temperature

intervals used in this investigation, the phase transition from the orthorhombic to the cubic phase appears to be continuous, although this cannot be the case as the two primary order parameters in the orthorhombic phase (q_2, q_4) (Carpenter et al., 2001; Carpenter 2007) have different symmetries (Tolédano and Tolédano, 1987). Despite this clear violation of Landau's theory for continuous phase transitions, Zhao et al (1993b) have derived critical phenomena associated with the orthorhombic – cubic phase transition, apparently finding both the in-phase, and the anti-phase tilt to have the identical critical exponent of 0.25.

In-situ, high temperature, high pressure experiments carried out on perovskite-structured $MgSiO_3$ has found a structural phase transition to the $CaIrO_3$ structure type at temperatures and pressures that correspond to the onset of the D□ layer within the Earth (120 GPa, 2500 K) (Murakami et al. 2004). Experimental investigations at this temperature and pressure are exceptionally difficult to carry out, and as a result, significant effort has been expended in studying isostructural compounds that undergo the perovskite - post-perovskite transition at more easily achievable temperatures and pressures (Martin et al. 2007; Lindsay-Scott et al. 2007, 2010, 2011; Lindsay-Scott 2011; Dobson et al. 2011). Neighborite was one of the first analog phases to be studied in detail, and has been found to undergo the post-perovskite transition at significantly lower pressure, although the transition pressure remains in dispute (Liu et al. 2005; Martin et al. 2006; Umemoto et al. 2006; Hustoft et al. 2008). Neighborite therefore remains an important analog phase for $MgSiO_3$, and as such, merits continuing, detailed investigations of the structure-property relationships in all its crystallographic phases.

In keeping with the continuous re-assessment of the physical properties of perovskite (and post-perovskite) structured neighborite, the understanding of the permitted space groups, and the thermodynamic basis of the structural phase transitions exhibited by the perovskite family as a whole, has been revolutionised in the past 15 years by the rigorous application of

group theoretical techniques for the first time by Howard and his co-workers (Howard and Carpenter 2009; Howard and Stokes 1998, 2002, 2005; Howard and Zhang 2004a, 2004b; Howard et al 2000, 2002, 2003; Stokes et al 2002; Zhang et al 2006, 2007). Supporting this crystallographic analysis, Carpenter (2007) has presented a complete Landau free energy expansion (Tolédano and Tolédano, 1987) for zone boundary tilted perovskites, to sixth order in the two symmetry independent primary order parameters, and to lowest order in the coupling between strain and the order parameters. For high temperature structural phase transitions, the standard Landau formalism has a temperature-dependent second order term (Tolédano and Tolédano, 1987; Carpenter et al. 2001), however for low temperature investigations, saturation of the primary order parameters has to be taken account of using a modified second order term (Salje et al. 1991; Carpenter 2007).

Parameterization of the crystal structures of perovskite phases in terms of the weights of condensed modes of the aristotype phase was initiated by Cochran and Zia (1968) for the two space groups *Pnma* and $R\bar{3}c$, and this work was subsequently furthered by Darlington (2002a, 2002b) to include seven more. More recently, these ideas have been reworked by Knight (2009a, 2009b) in terms of the amplitudes of the condensed modes of the aristotype phase that are consistent with the group-theoretical predictions of Howard and co-workers for the space groups of all zone-boundary tilted perovskite-structured, and elpasolite-structured phases (Howard and Stokes 1998, 2002, 2005; Howard et al. 2003). For space group *Pbnm*, or any one of its alternative settings, Knight (2011a) has shown how this parameterization can be used to both predict, and explain, the thermodynamic dependencies of the bond lengths and other structural distortions. The methodology has been applied to the crystallographic results from data collected at low temperatures on $KCaF_3$ (Knight 2011a), $CaTiO_3$ (Knight 2011b), $LaGaO_3$ (Knight 2012), and $BaCeO_3$ (Knight and Bonanos 2013),

and also from data collected at high temperatures, from the protonic conductor $SrCe_{0.95}Yb_{0.05}O_{\xi}$ (Knight 2011c).

In this paper we report a re-evaluation of the crystal structure and lattice metric of neighborite at low temperatures, between 9 K and 440 K. This work has been carried out using a larger set of data than has previously been reported (Mitchell et al. 2007), and, more importantly for a pseudosymmetric structure, the measurements have been made at significantly higher real space and reciprocal space resolution than before. Using mode decomposition techniques (Perez-Mato et al. 2010; Knight 2009a, 2011a) we report the structural basis for the thermal expansion of neighborite at low temperature. In addition, we estimate the Debye temperatures within the framework of the model proposed by Barron (1998), and determine the thermodynamic Grüneisen parameter in the temperature interval 313.15 K – 443.15 K. The conclusions drawn by Zhao et al. (1993a,b) from their comprehensive high temperature study of neighborite are critiqued in detail throughout this paper.

EXPERIMENTAL

10 g of neighborite was synthesised by solid state reaction of a stoichiometric mixture of pre-dried and ground NaF and MgF_2 powder at 750°C in air, for 15 h. Due to a small weight fraction of MgO in the MgF_2 precursor material, it was necessary to remove unreacted NaF by washing and drying the final material, before loading into a 15 mm thick, slab-geometry sample can equipped with vanadium front and back windows. Heat was supplied to the sample by a 100 W cartridge heater inserted in one wall of the sample can, and the temperature was controlled and monitored using an Rh/Fe sensor inserted into the opposite wall. Good thermal contact between heater and sensor and the container walls was achieved by using a copper-containing anti-seize compound. The body of the sample container,

147 including heater and sensor, was masked from the incident neutron beam using a gadolinium
148 shield to avoid contaminant Bragg peaks in the backscattering and 90° detector banks. The
149 sample was located in a Sumitomo RDK-415D top loading closed cycle refrigerator (CCR)
150 under 60 mbar of helium exchange gas, and cooled to 9 K. Powder neutron diffraction data
151 were collected in time-of-flight from 30 – 130 ms using the high resolution powder
152 diffractometer HRPD at the ISIS neutron spallation source. The initial data set was collected
153 at 9 K for 40 μAh, then 10 K, 15 K, and in 5 K steps to 440 K; all data collections above 9 K
154 were made for 10 μAh, approximately 15 minutes duration. Data collection was only
155 commenced once the control sensor had reached the set point temperature and a 5 minute
156 equilibration period had passed. The mean temperature variation was better ±0.1 K of the set
157 point temperature for all data collections.

158 The neutron time-of-flight data were focused, normalised to the incident beam flux
159 distribution, and corrected for self-shielding and wavelength-dependent absorption for a
160 sample with measured number density 9.83×10^{-3} Å^{-3}, and calculated cross sections of 19.04
161 b for scattering, and 0.62 b at 1.798 Å, for wavelength-dependent absorption. Normalised and
162 corrected data in the time-of-flight range 32 – 120 ms, corresponding to a *d*-spacing range of
163 ~0.64 – 2.4 Å in the high-resolution back scattering bank, and ~0.9 – 3.4 Å in the medium-
164 resolution 90° detector bank, were analysed using the Rietveld method, as implemented in the
165 GSAS suite of programs (Larson and Von Dreele, 1986). To calibrate the flightpaths for data
166 collected in the CCR, an additional data set was collected at 295.5 K with an added internal
167 standard of SRM640c silicon powder (lattice parameter: 5.431195(9)Å at 295.5 K).
168 Preliminary multiphase Rietveld refinement of the 9 K model showed the weight fraction of
169 MgO impurity to be 0.0223 and this value was kept fixed in the subsequent Rietveld
170 refinements. From the full set of eighty eight measurements, the 295 K data set was analysed
171 in detail first, using the lattice parameters and diffractometer constants derived from the

internal standard measurement, and the 300 K crystal structure for neighborite determined by Mitchell et al. (2007). Convergence from this initial model was rapid, and the result from the 295 K refinement was used as a seed for the 290 K and the 300 K refinements, the whole procedure being carried out iteratively down to 9 K, and up to 440 K. Typical results, in this case for the 9 K refinement are listed in Table 1, and the quality of fit to these data is shown in Figure 1.

RESULTS

In Figure 2 we plot the simulated diffraction patterns of neighborite at 300 K (Mitchell et al. 2007) over a small representative region between 2.0 and 2.5 Å, calculated using the resolution functions for HRPD (full line), and for DUAL-SPEC C2 (Chalk River) at a wavelength of 1.3282 Å (dashed line). It is immediately apparent that the real space resolution ($\Delta d/d$) of HRPD is approximately 10 times smaller than that for C2 at d = 2.24 Å, and, to first order, this resolution ($\sim 4.5 \times 10^{-4}$) is independent of the magnitude of the scattering vector (Windsor 1981). The minimum d spacing accessed by the high resolution detector bank on HRPD is ~0.64 Å, compared to a minimum of ~0.92 Å on the reactor diffractometer (Mitchell et al. 2007), and despite the short data collection times made on the time-of-flight instrument (~15 mins), the high count rate, the superior real space and reciprocal space resolution translates to improvements in precision over the work of Mitchell et al. (2007) by factors of ten in the estimated standard deviations (esds) of the unit cell, and factors of five in the esds of the fractional coordinates. It is therefore to be expected that the current study will be more sensitive to subtleties in the thermal evolution of the neighborite structure at low temperatures than the previous published work.

Unit Cell, Spontaneous Strains, Characteristic Temperatures, and Thermodynamic Grüneisen Parameter

196 The temperature variation of the three unit cell parameters is shown in Figure 3,
197 noting that the esds for all axes are smaller than the plotting symbols used. The *a* and *c* axes
198 both show the expected behavior for a simple dielectric material, saturation at low
199 temperature, and a linear thermal expansion coefficient at temperatures greater than room
200 temperature. These results are similar in form to those determined by Mitchell et al. (2007),
201 however the higher resolution HRPD measurements show the existence of a previously
202 unobserved region of negative thermal expansion for the *b* axis in the temperature interval 20
203 $K \leq T \leq 90$ K, which is illustrated as an inset in the Figure. Above 90 K, the *b* axis behaves in
204 a similar manner to the *a* and *c* axes, although the absolute variation in magnitude is
205 significantly smaller. Negative linear thermal expansion of the *b* axis for non-magnetically
206 ordered, centrosymmetric perovskite-structured materials with space group *Pbnm* is known in
207 at least two other compounds; in $KCaF_3$ (Knight, 2011a), where the effect is very large, and
208 equates to a strain ((*b*(T minimum)-*b*(0 K)/ *b*(0 K)) at the minimum (300 K) of -2.26×10^{-3},
209 and in $SrCeO_3$ (Knight, unpublished), where the strain at the minimum (150 K) is an order of
210 magnitude smaller, -1.46×10^{-4}. The effect in neighborite is smaller still, with a strain at the
211 minimum (90 K) of -7.1×10^{-5}. The temperatures at which low-temperature saturation of the
212 lattice parameters sets in are essentially indistinguishable for the *a*, and *c* axes, at ~50 K, for
213 the *b* axis, this temperature is found to be much lower, ~20 K.

214 In fitting their lattice parameter data, Mitchell et al. (2007) have made the use of
215 quartic polynomial expansions in temperature; however, these non-physical expressions have
216 finite derivatives at 0 K, and therefore violate the requirement for the volume thermal
217 expansion coefficient to become zero at this temperature. The full lines plotted on Figure 3
218 show weighted fits to the HRPD lattice parameter data using an expression related to an
219 Einstein internal energy function ($l(T) = l_0 + k_i / \left(\exp\left(\theta_i / T\right) - 1\right)$) that behaves in a
220 physically acceptable manner i.e. saturates at low temperatures and becomes linear at high

temperatures. It is clear, however, that a two term expression would be required to take into account the low temperature negative linear thermal expansion of the *b* axis ($l(T) = l_0 + \sum_{i=1}^{2} k_i / \left(\exp\left(\theta_i / T\right) - 1\right)$ with $k_1 < 0$, and $k_2 > 0$), and in practice, it was also found that a two term expression ($k_1 > 0$, and $k_2 > 0$) was also required to achieve good fitting for temperatures just above the saturation temperature for both the *a*, and the *c* axes. The high temperature limit of the derivative of the lattice parameter expression allows the high temperature linear thermal expansion coefficients to be estimated as $\alpha_a = 4.01(14) \times 10^{-5}\,K^{-1}$, $\alpha_b = 1.41(15) \times 10^{-5}\,K^{-1}$, and $\alpha_c = 3.08(11) \times 10^{-5}\,K^{-1}$, and these values are in excellent agreement with those experimentally determined below the phase transition temperature; $\alpha_a = 4.04(9) \times 10^{-5}\,K^{-1}$, $\alpha_b = 1.53(6) \times 10^{-5}\,K^{-1}$, and $\alpha_c = 3.06(4) \times 10^{-5}\,K^{-1}$ (Zhao et al. 1993a). The coefficients for fitting the lattice parameters, and their associated goodness of fits, are listed in Table 2.

Discussion of the decomposition of the crystal structure of neighborite in terms of the magnitudes of symmetry-adapted basis-vectors of irreducible representations (irreps) at the R, M, and X point of the aristotype Brillouin zone are made later in the paper. The symmetry-adapted spontaneous strains for space group *Pnma* are associated with irreps at the Γ point of the aristotype Brillouin zone; e_a, the volume strain transforms as the irrep Γ_1^+, e_{tx}, the tetragonal strain, as Γ_3^+, and e_4, the orthorhombic shear strain, as Γ_5^+ (Stokes and Hatch, 1988). In the absence of a reliable method to estimate the aristotype lattice parameter at low temperatures (a_0(T)), symmetry adapted spontaneous strains have been calculated from the linear stains using the expressions shown in McKnight et al. (2009) with the lattice parameters transformed into the *Pnma* setting, and making the approximation $a_0(T) \sim (V(T)/4)^{1/3}$, where V(T) is the unit cell volume. Whilst this method precludes the determination of the temperature dependence of the volume strain, it allows estimation of the

tetragonal and orthorhombic shear strains that may be compared to the equivalent results deduced from high temperature data, where extrapolation of the aristotype lattice parameter is exact. This comparison is illustrated in Figure 4 using unpublished high temperature data for neighborite collected on HRPD. It is clear from these Figures that the strains derived from the lattice parameter approximation used for the low temperature data are in good agreement with those calculated from the high temperature data, with only a small mismatch existing in the overlap region for e_{tx}. Furthermore, the low temperature strains vary as a function of the two order parameters q_2, and q_4, as predicted using the renormalized Landau free energy expansion derived by Carpenter (2007), and detailed in McKnight et al. (2009). The predicted behaviour at higher temperatures, based on fitting the low temperature results to the expressions given in McKnight et al. (2009), are found to be only in approximate correspondence with the experimental data. It is probable that this disagreement lies with the maximum order of the invariant polynomials considered by Carpenter (2007) in his Landau expansion. Evidence for this may be found in the thermal evolution of the three spontaneous strains in $KCaF_3$ in space group *Pbnm* (Knight and Howard, unpublished), where it was found necessary to include quartic terms of the order parameters to fit the strain data precisely. Detailed discussion of this point is beyond the scope of this current paper, but will be briefly returned to in the section concerning critical behaviour in neighborite.

The ability to derive useful thermodynamic quantities from the fitting of low temperature unit cell volume data, using first and second order Grüneisen approximations in conjunction with simple statistical mechanical models (Wallace 1972), has been pioneered in the Earth Sciences by Wood, and in the Planetary Sciences by Fortes; a representative sample of references to the methodologies used are given here (Vočadlo et al. 2002; Wood et al. 2002, 2004; Lindsay-Scott et al. 2011; Fortes et al. 2003; Fortes et al. 2008; Fortes et al. 2009). Recently, Knight (2012) and Knight and Bonanos (2013) have shown that in the

specific cases of the perovskite-structured compounds $LaGaO_3$ and $BaCeO_3$, the characteristic temperatures that can be derived from these fits are potentially unreliable when compared to those derived from independent fitting of calorimetric measurements. As a result Knight (2012) has recommended that for self-consistent results, the unit cell volume and the isochoric heat capacity (measured over the same, or a similar temperature interval) should be fitted simultaneously to the same statistical mechanical model. In the case of neighborite, we lack experimental measurements of the low temperature isobaric heat capacity, and hence the characteristic temperatures that are reported in this investigation are based solely on unit cell volume data, and hence should be considered as estimations to be confirmed, or improved, by subsequent low-temperature calorimetric measurements.

The temperature-dependence of the unit cell volume in the first order Grüneisen approximation is given by $V(T) = V_0 + \gamma U(T) / K_0$, where V_0 is the volume at 0 K, γ is a Grüneisen constant, K_0 is the isothermal bulk modulus, and $U(T)$ is the internal energy function (Wallace, 1972). The unit cell volume and a weighted fit based on a Debye internal energy function (Reif, 1965), are shown in Figure 5, noting the esds associated with the unit cell volumes are smaller than the plotting symbols used. The unit cell volume shows a similar temperature variation to the lattice parameters *a* and, *c*, and exhibits saturation for temperatures below ~50 K, with an estimated high temperature thermal expansion coefficient of $8.73(13) \times 10^{-5}\ K^{-1}$ which is in good agreement with the experimental work of Zhao et al. (1993a). Again it was found necessary to use a two term internal energy function, in this case weighted in the ratio 1:2 (Barron 1998; Knight 2012; Knight and Bonanos 2013), to satisfactorily fit the volume data close to the saturation temperature. Within the model of Barron, each of the Debye terms is associated with a unique Grüneisen constant, and the improvement in the degree of fitting the volume data to the more complex model can be appreciated by comparing the reduced χ^2 for the two fits; 427 for a single Debye term, and 2,

for two Debye terms. Based on the fitting results, the characteristic Debye temperatures for neighborite are 369(2) K and 1055(14) K, with associated Grüneisen constants of 3.23(6), and 1.11(1), respectively. The volume at 0 K was determined as 222.4935(4) $Å^3$, and the Grüneisen constants were calculated assuming an isothermal bulk modulus of 76.5 GPa (Martin et al. 2006). A single Debye term fit to the same data gave a Debye temperature of 510(4) K, V_0 = 222.524(5) $Å^3$, and a Grüneisen constant of 1.64(1).

The thermodynamic Grüneisen parameter is defined by the expression

$$\gamma_{th}(T) = \frac{\alpha(T) K_0(T) V_m(T)}{C_V(T)} \approx \frac{\alpha(T) K_0 V_m(T)}{C_P(T) - T\alpha^2(T) K_0 V_m(T)}$$ where the bulk modulus (K_0) is assumed to be temperature independent, C_V is the isochoric heat capacity, C_P is the isobaric heat capacity, α is the volume expansivity, and V_m is the molar volume. Although to our knowledge, the low temperature isobaric heat capacity of $NaMgF_3$ has not been measured, results in the temperature interval 313.15 K to 1153.15 K exist from a differential scanning calorimetry determination (Topor et al. 1997). From these data, we have determined the temperature variation of the thermodynamic Grüneisen parameter between 313.15 K and 443.15 K, using the expression shown above, the bulk modulus determined by Martin et al. (2006), and the two-term Debye parameterization to derive both the temperature dependent molar volume, and the volume expansion coefficient. These results are shown in Figure 6 (black full circles) where γ_{th} varies from ~1.75, at 313.15 K, to ~1.62, at 443.15 K, and is in agreement with the value derived from fitting the unit cell volume to a single Debye internal energy function. For comparison, γ_{th} for $CaTiO_3$ (Knight 2011b) is shown on the same plot (as open circles) and exhibits the same monotonic decrease from the lowest temperature as $NaMgF_3$. Whether the detailed low-temperature behaviour of the thermodynamic Grüneisen parameter of neighborite is similar to that of $CaTiO_3$, i.e. rising to a maximum at ~100 K before sharply reducing, we are not in a strong position to speculate. However, taking the

319 magnitudes of the Grüneisen constants derived from the two-term Debye fitting at face value,
320 a similar temperature variation would seem probable.

321 Crystal Structure

322 **Mode decomposition.** The fractional coordinates and lattice parameters for
323 neighborite at each temperature have been recast as the amplitudes of the seven symmetry-
324 adapted basis-vectors of the ideal aristotype phase that are consistent with space group *Pbnm*
325 (Cochran and Zia 1968; Darlington 2002b; Knight 2009a, 2011a, 2011b, 2011c, 2012; Knight
326 and Bonanos 2013). The advantage of mode decomposition for the analysis of
327 pseudosymmetric crystal structures is well documented (Perez-Mato et al. 2010), however in
328 the case of perovskites it has the particular advantage of permitting the displacements
329 associated with the primary order parameters i.e. those interpreted as in-phase/anti-phase
330 octahedral tilts to be determined independently of the effects of octahedral distortion. The
331 order parameters for centrosymmetric perovskite-structured phases (ABC_3) undergoing zone-
332 boundary phase transitions are proportional to the amplitudes of the symmetry-adapted basis-
333 vectors of the cubic aristotype phase that transform, either as the irreducible irrep R_4^+, and/or
334 M_3^+ (Cowley 1964). The mode displacements associated with the irrep R_4^+ are equivalent to
335 the anti-phase tilts of the BC_6 octahedra, as described by Glazer (1972); those associated with
336 M_3^+ are equivalent to the in-phase tilts of the BC_6 octahedra (Glazer 1972). Figure 7 shows the
337 temperature variation of the seven mode amplitudes for neighborite; note that the esds are
338 calculated from variance terms only. Figures 7a and 7b show the displacement amplitudes
339 associated with the Na site that transform as the basis vectors of the irreps R_5^+ and X_5^+
340 respectively; Figures 7c – 7g show the displacements associated with the anions. Figures 7c
341 and 7d illustrate the amplitudes associated with the primary order parameters, whilst Figures
342 7e – 7g show the amplitudes of the octahedral distortion modes that transform as the basis

vectors of the irreps X_5^+, M_2^+, and R_5^+ respectively. It is clear from the Figure that all modes have an appreciable magnitude, including that associated with M_2^+, which was found to be absent in $CaTiO_3$ at room temperature (Knight 2011b). This mode is generally found to have the smallest amplitude of the three octahedral distortive modes and has only previously been found to have a significant magnitude in B-site, Jahn-Teller distorted systems (Howard and Carpenter 2009).

Zhao et al. (1993a) presented tilt angles for neighborite derived using two methodologies: (i) from the unit cell parameters, termed macro, and calculated using expressions derived by O'Keeffe and Hyde (1977), and (ii), termed micro, derived from the fractional coordinates, or the C – B – C bond angles. Throughout the whole of the temperature range studied in this current investigation, the agreement in the calculated tilt angles between the two procedures was found to be poor. However, such a disagreement between the two methods is hardly surprising, as O'Keeffe and Hyde (1977) pointed out, their analysis was only applicable in systems exhibiting undistorted octahedra, which is clearly not the case in neighborite at either low, or high temperatures. Furthermore, it should be noted that the micro equations presented by Zhao et al. (1993a) represent only a slightly better approximation, as they do not correctly take into account the three octahedral distortive modes, which, as we have discussed above, have non-negligible amplitudes. For an accurate determination of the order parameters in perovskite-structured phases, that have the potential to be used in Landau free energy expansions (Tolédano and Tolédano, 1987; Salje, 1990; Carpenter et al. 2001; Carpenter 2007; Zhao et al. 1993b), it is necessary to decompose the crystal structure in terms of the amplitudes of the symmetry-adapted basis-vectors of the aristotype phase (Perez-Mato et al. 2010).

The full lines in Figure 7 show fits to the mode amplitude data using a variety of parameterizations, which can subsequently be used to determine the temperature-dependence of the Na – F, and Mg – F bond lengths (Knight 2011a). Figures 7a, 7b, 7e, 7g show the results of fitting to a single term saturation function identical to that described for fitting the unit cell data. The octahedral tilt amplitudes, shown in Figures 7c and 7d, have been fitted to the identical function for bond length parameterization, but the lines on the Figure are derived from fitting to critical behaviour with saturation which will be discussed in detail later; there is no appreciable difference in goodness of fit between the two alternative approaches. The data shown in Figure 7f have been fitted to a straight line.

Translations of the A cation from its aristotype position are dominated by the displacement that transforms as the irrep X_5^+, which is a factor of ~4 times larger than the displacement associated with the irrep R_5^+. The estimated temperatures at which the two displacements extrapolate to zero magnitude are in poor agreement, 1158 K (R_5^+) and 1727 K (X_5^+), and hence cannot be used to estimate the structural phase transition temperature to the aristotype structure, indeed that associated with X_5^+ exceeds the 1 atm melting point of $NaMgF_3$ of 1303 K (Topor et al. 1997). Displacements at the anion site are dominated by the two modes related to the octahedral tilt angles, with the principal distortive mode associated with the irrep X_5^+, a factor of 1/3 smaller. As in the case of the cation displacements, extrapolated temperatures to the zero magnitude give unreasonable estimates of the transition temperature to the cubic phase.

Bond lengths. The temperature-dependence of the Na – F bond lengths are illustrated in Figure 8, with the full lines showing the calculated behaviour based on the parameterisation of the modes as described above (Knight 2011a). In all cases, the agreement

between the observed and the parameterized bond length is excellent. It should be noted however, that when compared to the current investigation, the magnitudes of the esds of the bond lengths and angles quoted for the synchrotron study of neighborite at high temperature in Table 3 of Zhao et al. (1993a) are in significant disagreement. For the neutron diffraction refinement, esds of ~2×10^{-4} in the fractional coordinates, and ~2×10^{-5} Å in the lattice parameters are found, and the resultant esd for the Na – F1 bond lengths is of the order ~1×10^{-3} Å. As the esds in the fractional coordinates and the unit cell of the synchrotron study are poorer than the neutron diffraction results reported here, the esds in the Na – F and Mg – F bond lengths tabulated in Zhao et al. (1993a), of the order of 3×10^{-5} Å, are wholly inconsistent with their quoted errors. It is not entirely clear how these discrepancies have arisen, however the esds on the bond lengths are of the correct order of magnitude to be purely derived from the estimated errors associated with the unit cell without taking into account those related to the fractional coordinates.

Using the nomenclature of Knight (2011a) to distinguish the twelve fluorine nearest neighbors to the sodium site, the 300 K Na – F bond thermal expansion coefficients are in the order Na – F1(1') (9.3×10^{-5} K^{-1}) > Na – F2(6) (8.2×10^{-5} K^{-1}) > Na – F1(3') (4.3×10^{-5} K^{-1}) > Na – F2(3) (4.2×10^{-5} K^{-1}) > Na – F2(5) (9.5×10^{-6} K^{-1}) for the bonded interactions, and | Na – F1(1) | (7.5×10^{-5} K^{-1}) > | Na – F2(1) | (4.7×10^{-5} K^{-1}) > Na – F1(3) (2.4×10^{-6} K^{-1}) for the non-bonded interactions. For a bond vector $\mathbf{r} = r_x\mathbf{i} + r_y\mathbf{j} + r_z\mathbf{k}$ with orthonormal basis $\mathbf{i}$, $\mathbf{j}$, $\mathbf{k}$, ($\mathbf{i} \parallel \hat{\boldsymbol{a}}, \mathbf{j} \parallel \hat{\boldsymbol{b}}, \mathbf{k} \parallel \hat{\boldsymbol{c}}$) the bond thermal expansion coefficient is given by $\frac{1}{r}\frac{dr}{dt} = \left[\left(\frac{r_x}{r^2}\right)\frac{dr_x}{dt} + \left(\frac{r_y}{r^2}\right)\frac{dr_y}{dt} + \left(\frac{r_z}{r^2}\right)\frac{dr_z}{dt}\right]$, and hence parameterizing the bond vector using mode decomposition allows the structural basis for the changes in bond length with temperature to be determined.

Within the mirror plane, the bond Na – F1(1') is principally resolved along ***b***, and, despite the relatively low linear thermal expansion coefficient for this axial direction at 300 K, the bond thermal expansivity is the highest due to the sympathetic displacements of the anion and cation with irrep X_5^+. The order and the percentage contributions to the total bond thermal expansion coefficient are given by X_5^+(A site) (~69%) > $|R_4^+|$(~-13%) > *b* axis (~12%) > X_5^+ (~36%) > $|R_5^+|$(A site) (~-6%) > R_5^+ (~2%). The effect of displacements associated with the anti-phase tilt is negative, a factor five times smaller than that associated with the anion displacement with irrep X_5^+, and can be seen to be essentially nullified by the thermal expansion of the *b* axis. By way of contrast, the thermal expansivity of the bond Na – F1(3'), which is principally resolved along ***a***, is dominated by the sympathetic displacements from the anti-phase tilt and the thermal expansion of the *a* axis. In this case, the order of contributions is given by R_4^+ (~132%) > *a* axis (~90%) > $|R_5^+|$(A site) (~-60%) > $|X_5^+|$(A site) (~-27%) > $|R_5^+|$(~-20%) > $|X_5^+|$(~-14%). The expansivity of this bond is therefore significantly reduced by the antipathetic displacements associated with the two cation modes. The strong negative expansivity of the non-bonded interaction Na – F1(1) is attributable to the anion and cation displacements associated with the irrep X_5^+, whilst the negligible change, over the whole temperature range, in the Na – F1(3) non-bonded distance arises from the cancellation of the positive contributions from the *a* axis and the anion displacement that transforms as the irrep R_5^+ by the displacement from the anti-phase tilt.

As the bond vectors from the cation to the anions labelled F2 lie out of the mirror plane, deducing the structural basis for the bond thermal expansivities is by necessity more complex to determine than those to F1, due to the larger number of contributing terms. For

435 the 300 K expansion of the bond Na – F2(6), to first order the contributions from the thermal
436 expansion of the b axis and the anion displacements associated with the irreps M_2^+ and R_5^+ are
437 small enough to be ignored. Significant positive contributions are found from the
438 displacements in the order X_5^+ (A site) (~40%) > R_4^+ (~26%) > R_5^+ (A site) (~17%) > *c* axis
439 (~14%) > *a* axis (~12%). The overall bond expansivity is reduced by two independent
440 negative contributions from the in-phase tilt at ~-9% and ~-8%. The intermediate thermal
441 expansion coefficient of the bond Na – F2(3) can be shown to arise from the large
442 antipathetic displacements of the cation with irrep X_5^+ which reduces the overall magnitude by
443 approximately one half. Displacement magnitudes are found to be in the order $|X_5^+|$ (A site)
444 (~-98%) > R_4^+ (~64%) > *c* axis (34%) > R_5^+ (A site) (~27%) > *a* axis (~20%) > M_3^+ (~19%) >
445 M_3^+ (~14%) > R_5^+ (~9%) > *b* axis (~8%). In a similar manner to that found for the non-
446 bonded distance Na – F1(3), the almost negligible thermal expansion of the Na – F2(5) bond
447 is related to the near cancellation of all contributing terms; $|R_4^+|$ (~-305%) > X_5^+ (A site)
448 (~205%) > *c* axis (160%) > $|R_5^+|$ (A site) (~-99%) > *a* axis (~74%) > M_3^+ (~51%) > $|R_5^+|$
449 (~-45%) > M_3^+ (~40%) > *b* axis (~18%).

450 The temperature-dependence of the bond lengths for the three independent Mg – F
451 distances is illustrated in Figure 9, with the predicted variation derived from mode
452 parameterization shown as the full lines. Thermal expansion coefficients for the three bond
453 lengths are low, similar, in the range 6.1 – 7.4 × 10^{-6} K^{-1}, and a factor of ~10 smaller than
454 those determined for Na – F. Expansion of the bond Mg – F1(1) is dominated by the thermal
455 expansion of the *c* axis, the effect of the anti-phase tilt is found to reduce the expansion
456 coefficient by 2/3 (*c* axis (~328%) > $|R_4^+|$ (~-218%) > $|X_5^+|$ (~-43%) > R_5^+ (~32%)). The
457 thermal expansion of the two Mg – F2 bond lengths is primarily driven by increases in the *a*,

458 and *b* axes, but in both cases this is reduced by near-cancellation of displacements from two
459 independent components on the in-phase tilt. The contribution of the anti-phase tilt is strongly
460 negative in both cases, and as the bond expansion coefficients are so small, even
461 displacements associated with the irrep M_2^+ cannot be ignored. For Mg – F2(1), the order of
462 displacement magnitudes are: *a* axis (~298%) > $|M_3^+|$ (~-206%) > M_3^+ (~145%) > $|R_4^+$
463 $|$(~-135%) > *b* axis (~66%) > $|M_2^+|$ (~-28%) > $|R_5^+|$ (A site) (~-20%) > $|M_2^+|$ (~-
464 20%); for Mg – F2(4) the following order is found: $|M_3^+|$ (~-170%) > *a* axis (~165%) >
465 M_3^+ (~114%) > $|R_4^+|$(~-114%) > *b* axis (~78%) > M_2^+ (~23%) > $|R_5^+|$ (A site) (~-16%) >
466 M_2^+ (~16%).

467 **Atomic displacement parameters.** The isotropic or isotropic equivalent atomic
468 displacement parameters for all independent atoms are illustrated in Figure 10. Isotropic
469 displacement parameters were refined for F1 up to a temperature of 235 K, and for F2, up to a
470 temperature of 185 K; no obvious discontinuity can be seen in these results at the
471 temperatures that relate to the increase in the complexity of the structural model. The full
472 lines on the Figure show weighted fits to the modified Debye model of Wood et al. (2002),
473 which allows the zero-point term to be additional refinable parameter. The vibrational Debye
474 temperature for the octahedrally coordinated Mg cation, 588(5) K, is significantly larger than
475 that of the 8-fold coordinated Na cation, 346(1) K which reflects the greater structural
476 degrees of freedom in the larger, softer site. The two values are comparable with those found
477 for the two cation sites in cubic $KMgF_3$ (K, 305(2) K; Mg 522(4) K) (Wood et al. 2002) over
478 the temperature range 373 K to 1223 K. Debye temperatures for the anions in neighborite are
479 similar, 455(3) K for F1, and 477(3) K for F2, and compare well with the weighted average
480 of the individual vibrational Debye temperatures for the anisotropic refinements of the
481 fluorine anion in $KMgF_3$ (u_{11} = 581(7) K, u_{33} = 422(2) K; F: 1/2, 0, 0). Refined zero point

terms were found to be: Na, 0.00450(7) $Å^2$; Mg, 0.00061(6) $Å^2$; F1, 0.00169(6) $Å^2$; F2, 0.00242(4) $Å^2$, compared to calculated values derived from the refined vibrational Debye temperatures: Na, 0.0046 $Å^2$; Mg, 0.0025 $Å^2$; F1, 0.0042 $Å^2$; F2, 0.0040 $Å^2$.

Polyhedral Volumes. To compare the polyhedral volumes and their associated thermal expansion properties, we have plotted temperature-dependences of the volume strains, $(V(T)-V_0)/V_0$, and the thermal expansion coefficients on the same graph, Figure 11. From saturated values of 24.364(1) $Å^3$ and 10.3117(3) $Å^3$ at 9 K, for the A site, and B site respectively, both polyhedral volumes increase with increasing temperature, with the volume expansivity of the NaF_8 site exceeding that of the MgF_6 site by nearly a factor of 4 by 440 K. The estimated high temperature volume expansion coefficient for the NaF_8 site is large 1.15×10^{-4} K^{-1}, almost double that determined for the A sites in the oxide perovskites $CaTiO_3$ (Knight 2011b), $LaGaO_3$ (Knight 2012), $BaCeO_3$ (Knight and Bonanos 2013), and $SrCeO_3$ (Knight unpublished), and is comparable with the measured volume expansivity of cubic NaF, 1.13×10^{-4} K^{-1} (Deshpande 1961).

In the aristotype phase of a perovskite-structured phase, the ratio of the dodecahedral (A site) to the octahedral (B site) polyhedral volume is 5, and by necessity, is independent of any thermodynamic variable. On entering a lower symmetry zone-boundary tilted hettotype phase, this ratio reduces as the coordination of the A site reduces from 12, and there now exists a component of non-bonded free volume within the unit cell (Mitchell 2002). In $NaMgF_3$, the unit cell volume can be broken down into NaF_8 (A site volume) ~44% > non-bonded ~38% > MgF_6 (B site volume) ~18%, and the ratio of the A site volume to the B site volume is greatly reduced from 5 to ~2.4. On heating a non-magnetically ordered perovskite-structured phase in space group *Pbnm* from ultra-low temperatures to room temperature, the A site volume always increases, however the volume corresponding to the B site can either increase ($CaTiO_3$, $LaGaO_3$, $NaMgF_3$), remain constant ($SrCeO_3$), or decrease ($BaCeO_3$,

507 $KCaF_3$). Due to bonding requirements of the B site, the magnitude of the polyhedral volume
508 expansion coefficient of the A site is always significantly greater than of the octahedral site,
509 and hence the polyhedral volume ratio increases with increasing temperature. In the case of
510 neighborite, this ratio increases from 2.36 at 9 K, to 2.43 at 440 K, extrapolation of this ratio
511 to 5 to determine the phase transition temperature to the aristotype phase gives a non-physical
512 estimate, significantly above the 1 atm. melting point.

513

514 Critical Behaviour

515 Carpenter (2007) has presented a Landau free energy expansion for crystal structures
516 in space group $Pm\bar{3}m$ that transform to structures with isotropy subgroups associated with
517 the irreps M_3^+ and R_4^+. The Landau potential is expanded to sixth order in the primary order
518 parameters, and to lowest order in the strain-order parameter coupling terms, and has been
519 successfully used to fully characterise the tetragonal (*I*4/*mcm*) to cubic ($Pm\bar{3}m$) phase
520 transition in $SrTiO_3$. Taking into account low temperature saturation, the equilibrium
521 evolution of the order parameters q_2 (order parameter related to M_3^+) and q_4 (order parameter
522 related to R_4^+) in space group *Pnma*, or any alternative setting of *Pnma*, are given by the
523 solutions of

$$\frac{\partial G}{\partial q_4} = 0 = 2a_2\Theta_{s2}\left[\coth\left(\frac{\Theta_{s2}}{T}\right) - \coth\left(\frac{\Theta_{s2}}{T_{c2}}\right)\right]$$
$$+2b_2q_4^2+4c_2q_4^4+4\lambda^* q_2^2 + \frac{4\lambda_5^2(\lambda_6+\lambda_7)q_2^2q_4^2}{C_{44}^{0\ 2}}$$

524

$$\frac{\partial G}{\partial q_2} = 0 = a_1\Theta_{s1}\left[\coth\left(\frac{\Theta_{s1}}{T}\right) - \coth\left(\frac{\Theta_{s1}}{T_{c1}}\right)\right]$$
$$+b_1q_2^2+c_1q_2^4+4\lambda^* q_4^2 + \frac{2\lambda_5^2(\lambda_6+\lambda_7)q_4^4}{C_{44}^{0\ 2}}$$

525 where T_{c1}, T_{c2} are critical temperatures; Θ_{s1}, Θ_{s2} are saturation temperatures; a_1, a_2 are normal
526 Landau coefficients; b_1, b_2, c_1, c_2 are renormalized Landau coefficients; λ^*, λ_5, λ_6, λ_7 are
527 coupling coefficients, and C_{44}^0 is the bare elastic constant of the cubic phase; see Carpenter
528 (2007) for the full expression and the derivation of these equations. Zhao et al. (1993b)
529 presented a pair of alternative expressions to explain the critical behaviour of neighborite at
530 high temperature, but these are based on a simpler, less rigorous coupling scheme (Salje
531 1990), and included the assumption that fourth order terms in the order parameters were
532 small enough to be ignored:

$$\frac{\partial G}{\partial q_4} = 0 = A_1(T - T_{c1})q_4 + C_1q_4^5 + \lambda q_4q_2^2$$

533

$$\frac{\partial G}{\partial q_2} = 0 = A_2(T - T_{c2})q_2 + C_2q_2^5 + \lambda q_4^2q_2$$

534 These two sets of equations are *coupled*, *simultaneous*, and *non-linear*, and therefore only
535 have closed solutions for particular values of the Landau coefficients and coupling constants.
536 However, Zhao et al. (1993b) have presented solutions to these equations as if they were
537 *uncoupled*, and *independent*, and on the basis of this mathematical error, have claimed that
538 both the in-phase tilt and anti-phase tilt exhibit tricritical behaviour, i.e. the critical exponent
539 for both order parameters is simultaneously 0.25. As we have noted earlier, the order

parameters have different symmetries, and therefore a continuous phase transition from the orthorhombic phase to the cubic aristotype violates Landau theory, and hence the conclusions drawn by Zhao et al. (1993b) are formally invalid.

The expressions derived by Carpenter are significantly more complex, and are therefore more challenging to solve. However the fit to the basis vector amplitude that corresponds to the anti-phase tilt, shown in Figure 7c, is based on the simplest set of assumptions; that the coupling terms are small enough to be ignored, and that the Landau coefficients b1, and b2 are zero. The quality of fit to the data indicates the anti-phase tilt to exhibit tricritical behaviour at low temperatures, with refined values of 95(3) K, and 1198(6) K being found for the saturation temperature, and the critical temperature respectively. Comparison of Figures 7c and 7d shows the behaviour of the in-phase tilt is not tricritical in nature, contrary to the conclusions of Zhao et al. (1993b), and in Figure 12 we show that the square of the displacement of the in-phase tilt is linear in the displacement of the anti-phase tilt. The full line shows a straight line fit to these data, without any constraints, and includes the long saturation region of the in-phase tilt; the dashed line shows a fit to the data for an anti-phase displacement greater than 0.35, and constrained to pass through the origin. From these results, there is good evidence for a coupling of the square of the in-phase tilt to the anti-phase tilt, and the full line shown in Figure 7d shows the evolution of the in-phase tilt with temperature, assuming saturation at low temperature and a fixed critical exponent of 0.125.

Strong supporting evidence for the values of these critical exponents can be found in the evolution of the spontaneous strains e_{tx}, and e_4 with temperature. The full lines plotted in Figures 4a,b illustrate the predicted behaviour of these two strains, and are based on initial fits to the experimental spontaneous strains according to the expressions presented in McKnight et al. (2009), using the amplitudes of the two order parameters derived by mode

565 decomposition. The predicted strain variations were then calculated using the coefficients
566 from this fitting procedure, the values of the critical and saturated temperatures from fitting
567 the order parameter temperature variation, and assuming the critical exponents 0.25 and
568 0.125 for q_4, and q_2 respectively. The agreement between the calculated and predicted strains
569 is excellent.

570 Taking into account higher order invariant polynomials than were considered by
571 Carpenter (2007), we note that linear quadratic coupling of the form $q_4 q_2^2$ is not allowed by
572 symmetry, but the term containing $q_4^2 q_2^4$ is permitted (Salje and Devarajan, 1986). The
573 behaviour of the anti-phase tilt is therefore close to tricritical in nature, i.e. q_4^4 is linear in
574 temperature; the q_2^8 behaviour simply follows from coupling to the q_4 term as $q_4^2 q_2^4$, and hence
575 the phase transition apparently occurs as if there was only a single instability at the R point of
576 the cubic Brillouin zone. A reinvestigation of neighborite at high temperatures using high
577 resolution powder neutron diffractometry and mode decomposition to correctly determine the
578 values of q_2 and q_4 could confirm this conjecture, however the marked bond-shortening of the
579 cation – anion bonds observed by Zhao et al. (1993a,b) may preclude this methodology, and
580 an analysis based on the intensities of superlattice reflections may be more appropriate.

581

582 **IMPLICATIONS**

583 Structural phase transitions and critical behaviour in perovskite-structured compounds
584 has remained an active area of research in condensed matter physics for nearly fifty years
585 (Cowley, 1964; Cochran and Zia, 1968; Howard et al. 2000, 2002), however, it is only within
586 the past fifteen years that crystallographic instrumentation and parametric data analysis
587 techniques have reached a stage where phenomenological conclusions from Landau theory

588 can be tested in a simple manner (Tolédano and Tolédano 1987; Salje 1990; Howard et al.
589 2000, 2002; Howard and Stokes 1998, 2002; Carpenter et al. 2001; Carpenter 2007; Perez-
590 Mato et al. 2010).

591 It is now generally accepted that the major perovskite phase of the Earth's lower
592 mantle, $MgSiO_3$, remains orthorhombic, space group *Pbnm*, from its formation conditions
593 until near the core-mantle boundary (Murakami et al. 2004), and hence potential critical
594 behavior inferred by studying the analog phase neighborite might not appear to be directly
595 relevant to the Earth Sciences. This, however, is not true for the behaviour of $CaSiO_3$
596 perovskite, believed to be the third most abundant lower mantle mineral phase, and for which
597 there is no agreed consensus concerning structural phase transition temperatures, crystal
598 system, or space group (Kombayashi et al. 2007; Li et al. 2006; Adams and Oganov 2006;
599 Uchida et al. 2009). Furthermore, inferring the nature of ferroelasticity in these oxide systems
600 via the use of analog phases, has relevance to geophysical interpretation, for example, in the
601 understanding of seismic anomalies (Kombayashi et al. 2007), and seismic attenuation (Li
602 and Weidner 2012).

603

604 **ACKNOWLEDGEMENTS**

605 I am grateful for the careful and thorough reviews of this manuscript by Professors
606 Roger Mitchell and Michael Carpenter which has led to substantial improvements in the final
607 paper and to Dr. Alexandra Friedrich for her editorial assistance. Dr Ian Wood is thanked for
608 the many helpful discussions concerning the behavior of neighborite at low and high
609 temperatures.

610 This paper is dedicated to the memory of my friend and collaborator, Charles
611 Nicholas Wright Darlington (1945 – 2013), perovskite crystallographer and solid-state
612 physicist, formerly of the University of Birmingham, U.K.

613

614 **REFERENCES CITED**

615 Adams, D.J. and Oganov, A.R. (2006) Ab initio molecular dynamics study of $CaSiO_3$
616 perovskite at P-T conditions of Earth's lower mantle. Physical Review B, 73, 184106.

617 Anderson, N.H., Kjems, J.K., and Hayes, W. (1985) Ionic conductivity of the perovskites
618 $NaMgF_3$, $KMgF_3$ and $KZnF_3$ at high temperatures. Solid State Ionics, 17, 143 - 145.

619 Barron, T.H.K. (1998) CINDAS Data Series on Materials Properties I-4, 1.

620 Carpenter, M.A. (2007) Elastic anomalies accompanying phase transitions in $(Ca,Sr)TiO_3$
621 perovskites: Part I. Landau theory and a calibration for $SrTiO_3$. American Mineralogist, 92,
622 309 – 327.

623 Carpenter, M.A., Becerro, A.I. and Seifert, F. (2001) Strain analysis of phase transitions in
624 $(Ca,Sr)TiO_3$ perovskites. American Mineralogist, 86, 348 – 363.

625 Chao, E.C.T., Evans Jr., H.T., Skinner, B.J., and Milton, C. (1961) Neighborite, $NaMgF_3$, a
626 new mineral from the Green River Formation, South Ouray, Utah. American Mineralogist,
627 46, 379 – 393.

628 Cheeseman, P.A., and Angell, C.A. (1981) Fast ion conductivity in cubic perovskite
629 structures: An ion dynamic study of $NaMgF_3$. Solid State Ionics, 5, 597 - 600.

630 Cochran, W., and Zia, A. (1968) Structure and dynamics of perovskite-type crystals. Physica
631 Status Solidi, 25, 273 – 283.

Cowley, R.A. (1964) Lattice dynamics of $SrTiO_3$. Physical Review, 134, A981-A997.

Darlington, C.N.W. (2002a) Normal-mode analysis of the structures of perovskites with tilted octahedra. Acta Crystallographica A, 58, 66 – 71.

Darlington, C.N.W. (2002b) Normal-mode analysis of the structures of perovskites with tilted octahedra. Erratum. Acta Crystallographica A, 58, 299 – 300.

Deshpande, V.T. (1961) Thermal expansion of sodium fluoride and sodium bromide. Acta Crystallographica, 14, 794.

Dobson, D.P., Hunt, S.A., Lindsay-Scott, A., and Wood, I.G. (2011) Towards better analogues for $MgSiO_3$ post-perovskite: $NaCoF_3$ and $NaNiF_3$, two new recoverable fluoride post-perovskites. Physics of the Earth and Planetary Interiors, 189, 171 – 175.

Fortes, A.D., Wood, I.G., Brodholt, J.P., Alfredsson, M., Vočadlo, L., McGrady, G.S., and Knight, K.S. (2003) A high-resolution neutron powder diffraction study of ammonia dihydrate ($ND_3.2D_2O$) phase I. Journal of Chemical Physics, 119, 10806 - 10813.

Fortes, A.D., Wood, I.G., Vočadlo, L. Chapon, L.C., Knight, K.S., and Smith, R.I. (2008) Neutron powder diffraction studies of sulfuric acid hydrates. II. The structure, thermal expansion, incompressibility, and polymorphism of sulfuric acid tetrahydrate (D_2SO_4 $4D_2O$). The Journal of Chemical Physics, 128, 054506.

Fortes, A.D., Wood, I.G., Vočadlo, L., Knight, K.S., Marshall, W.G.,Tucker, M.G., and Fernandez-Alonso, F., (2009) Phase behaviour and thermoelastic properties of ammonia hydrate and ice polymorphs from 0 – 2 GPa. Journal of Applied Crystallography, 42, 846 - 866.

Glazer, A.M. (1972) The classification of tilted octahedra in perovskites. Acta Crystallographica B, 28, 3384 – 3392.

Howard, C.J., and Carpenter, M.A. (2009) Octahedral tilting in cation-ordered Jahn-Teller distorted perovskites – a group theoretical analysis. Acta Crystallographica B, 66, 40 – 50.

Howard, C.J., Kennedy, B.J., and Woodward, P.M. (2003) Ordered double perovskites – a group theoretical analysis. Acta Crystallographica B, 59, 463 – 471.

Howard, C.J., Knight, K.S., Kennedy, B.J., and Kisi, E.H. (2000) The structural phase transitions in strontium zirconate revisited. Journal of Physics: Condensed Matter, 12, L677 – L683.

Howard, C.J., Luca, V., and Knight, K.S. (2002) High-temperature phase transitions in tungsten oxide – the last word? Journal of Physics: Condensed Matter, 14, 377 – 387.

Howard, C.J., and Stokes, H.T. (1998) Group-theoretical analysis of octahedral tilting in perovskites. Acta Crystallographica B, 54, 782 – 789.

Howard, C.J., and Stokes, H.T. (2002) Group-theoretical analysis of octahedral tilting in perovskites. Erratum. Acta Crystallographica B, 58, 565.

Howard, C.J., and Stokes, H.T. (2005) Structures and phase transitions in perovskites – a group-theoretical approach. Acta Crystallographica A, 61, 93 - 111.

Howard, C.J., and Zhang, Z. (2004a) Structure for perovskites with layered ordering of the A-site cations. Acta Crystallographica B, 60, 249 - 251.

Howard, C.J., and Zhang, Z. (2004b) Structure for perovskites with layered ordering of the A-site cations. Erratum. Acta Crystallographica B, 60, 763.

Hustoft, J., Catalli, K., Shim, S.-H., Kubo, A., Prakapenka, V.B., and Kunz, M. (2008) Equation of state of $NaMgF_3$ postperovskite: Implication for the seismic velocity changes in the D□ region. Geophysical Research Letters, 35, L10309.

Kay, H.F., and Bailey, P.C. (1957) Structure and properties of $CaTiO_3$. Acta Crystallographica, 10, 219 – 226.

Knight, K.S. (2009a) Parameterization of the crystal structures of centrosymmetric zone-boundary-tilted perovskites: An analysis in terms of symmetry-adapted basis-vectors of the cubic aristotype phase. Canadian Mineralogist, 47, 381 – 400.

Knight, K.S. (2009b) Parameterization of the crystal structures of centrosymmetric elpasolite crystal structures in terms of symmetry-adapted basis-vectors of the cubic aristotype phase. Canadian Mineralogist, 47, 401 – 420.

Knight, K.S. (2011a) Centrosymmetric perovskite crystal structures with space group *Pbnm*: Crystallographic parameterization of $KCaF_3$ between 100 and 400 K in terms of the amplitudes of symmetry-adapted basis-vectors of the cubic aristotype phase. Canadian Mineralogist, 49, 793 – 808.

Knight, K.S. (2011b) Structural and thermoelastic properties of $CaTiO_3$ perovskite between 7 K and 400 K. Journal of Alloys and Compounds, 509, 6337 – 6345.

Knight, K.S. (2011c) Structural and thermoelastic study of the protonic conducting perovskite $SrCe_{0.95}Yb_{0.05}O_{\xi}$ (ξ~3) between 373 K and 1273 K. Journal of Electroceramics, 27, 143 – 153.

Knight, K.S. (2012) Low temperature thermoelastic and structural properties of $LaGaO_3$ perovskite in the *Pbnm* phase. Journal of Solid State Chemistry, 194, 286 – 296.

Knight, K.S., and Bonanos, N. (2013) Thermoelastic and structural properties of ionically conducting cerate perovskites: (I) $BaCeO_3$ at low temperature in the *Pbnm* phase. Solid State Ionics, 232, 112 – 122.

Kombayashi, T., Hirose, K., Sata, N., Ohishi, Y., and Dubrovinsky, L.S. (2007) Phase transition in $CaSiO_3$ perovskite. Earth and Planetary Science Letters, 260, 564 – 569.

Larson, A.C., and Von Dreele, R.B. (1986) Los Alamos National Laboratory Report LAUR 86-748.

Li, L., Weidner, D.J. (2012) Anelasticity and transient creep in $NaMgF_3$ perovskite at high pressure. Physics of the Earth and Planetary Interiors, 194 - 195, 98 – 106.

Li, L., Weidner, D.J., Brodholt, J., Alfe, D., Price, G.D., Caracas, R., and Wentzcovitch, R. (2006) Phase stability of $CaSiO_3$ perovskite at high pressure and temperature: insights from ab initio molecular dynamics. Physics of the Earth and Planetary Interiors, 155, 260 – 268.

Lindsay-Scott, A. (2011) Thermoelastic properties of post-perovskite phases, 336 p. Ph.D. thesis, University College, London.

Lindsay-Scott, A., Wood, I.G., Dobson, D.P. (2007) Thermal expansion of $CaIrO_3$ determined by X-ray powder diffraction. Physics of the Earth and Planetary Interiors, 162, 140 – 148.

Lindsay-Scott, A., Wood, I.G., Dobson, D.P., Vočadlo, L., Brodholt, J.P., Crichton, W., Hanfland, M., and Taniguchi, T. (2010) The isothermal equation of state of $CaPtO_3$ post-perovskite to 40 GPa. Physics of the Earth and Planetary Interiors, 182, 113 – 118.

Lindsay-Scott, A., Wood, I.G., Dobson, D.P., Vočadlo, L., Brodholt, Knight, K.S., Tucker, M.G., and Taniguchi, T. (2011) Thermoelastic properties and crystal structure of $CaPtO_3$

718 post-perovskite from 0 – 9 GPa and from 2 – 973 K. Journal of Applied Crystallography, 44,
719 999 – 1016.

720 Liu, H.-Z., Chen, J., Hu, J., Martin, C.D., Weidner, D.J., Hāusermann, D., and Mao, H.-K.
721 (2005) Octahedral tilting evolution and phase transition in orthorhombic $NaMgF_3$ perovskite
722 under pressure. Geophysical Research Letters, 32, L04304.

723 Martin, C.D., Crichton, W.A., Liu, H., Prakapenka, V., Chen, J., and Parise, J.B. (2006)
724 Phase transition and compressibility of $NaMgF_3$ (neighborite) in perovskite- and post-
725 perovskite-related structures. Geophysical Research Letters, 33, L11305.

726 Martin, C.D., Chapman, K.W., Chupas, P.J., Prakapenka, V., Lee, P.L., Shastri, S.D., and
727 Parise, J.B. (2007) Compression, thermal expansion, structure, and instability of $CaIrO_3$, the
728 structure model of $MgSiO_3$ post-perovskite. American Mineralogist, 92, 1048 – 1053.

729 McKnight, R.E.A., Howard, C.J., and Carpenter, M.A. (2009) Elastic anomalies associated
730 with transformation sequencies in perovskites: I. Strontium zirconate, $SrZrO_3$. Journal of
731 Physics: Condensed Matter, 21, 015901.

732 Mitchell, R.H. (2002) Perovskites modern and ancient, 318 p, Almaz Press, Ontario.

733 Mitchell, R.H., Alexander, M., Cranswick, L.M.D., and Swainson, I.P. (2007) A powder
734 neutron diffraction study of the fluoroperovskite $NaMgF_3$ (neighborite) from 300 K to 3.6 K.
735 Physics and Chemistry of Minerals, 34, 705 – 712.

736 Murakami, M., Hirose, K., Kawamura, K., Sata, N., and Ohishi, Y. (2004) Post-perovskite
737 phase transition in $MgSiO_3$. Science, 304, 855 – 858.

738 O'Keeffe, M., and Bovin, J-O (1979) Solid electrolyte behavior of $NaMgF_3$: geophysical
739 implications. Science, 206, 599 - 600.

O'Keeffe, M., Hyde, B.G. (1977) Some structures topologically related to cubic perovskite (E21), ReO_3 (D09) and Cu_3Au (L12). Acta Crystallographica B, 33, 3802 – 3813.

O'Keeffe, M., Hyde, B.G., and Bovin, J-O (1979) Contribution to the crystal chemistry of orthorhombic perovskites: $MgSiO_3$ and $NaMgF_3$. Physics and Chemistry of Minerals, 4, 299 - 305.

Perez-Mato, J.M., Orobengoa, D., and Aroyo, M.I. (2010) Mode crystallography of distorted structures. Acta Crystallographica A, 66, 558 – 590.

Reif, F. (1965) Fundamentals of statistical and thermal physics, 651 p., McGraw-Hill, New York.

Salje, E.K.H. (1990) Phase transitions in ferroelastic and co-elastic crystals, 300 p., Cambridge University Press, Cambridge.

Salje, E.K.H., Devarajan, V. (1986) Phase transitions in systems with strain-induced coupling between two order parameters. Phase Transitions, 6, 235 – 248.

Salje, E.K.H., Wruck, B., and Thomas, H. (1991) Order-parameter saturation and low-temperature extension of Landau theory. Zeitschrift für Physik B Condensed Matter, 82, 399 – 404.

Stokes, H.T. and Hatch, D.M. (1988) Isotropy subgroups of the 230 crystallographic space groups, 622 p., World Scientific Publishing, Singapore.

Stokes, H.T., Kisi, E.H., Hatch, D.M., and Howard, C.J. (2002) Group-theoretical analysis of octahedral tilting in ferroelectric perovskites. Acta Crystallographica B, 58, 934 - 938.

Tolédano, J-C., and Tolédano, P. (1987) The Landau theory of phase transitions, 451 p., World Scientific, Singapore.

762 Topor, L., Navrotsky, A., Zhao, Y., and Weidner, D.J. (1997) Thermochemistry of fluoride
763 perovskites: Heat capacity, enthalpy of formation, and phase transition of $NaMgF_3$. Journal of
764 Solid State Chemistry, 132, 131 – 138.

765 Uchida, T., Wang, Y., Nishiyama, N., Funakoshi, K., Kaneko, H., Nozawa, A., Von Dreele,
766 R.B., Rivers, M.L., Sutton, S.R., Yamada, A., Kunimoto, T., Irifune, T., Inoue, T., and Li, B.
767 (2009) Non-cubic symmetry of $CaSiO_3$ perovskite up to 18 GPa and 1600 K. Earth and
768 Planetary Science Letters, 282, 268 – 274.

769 Umemoto, K., Wentzcovitch, R.M., Weidner, D.J., and Parise, J.B. (2006) $NaMgF_3$: A low-
770 pressure analog of $MgSiO_3$. Geophysical Research Letters, 33, L15304.

771 Vočadlo, L., Knight, K.S., Price, G.D. and Wood, I.G. (2002) Thermal expansion and crystal
772 structure of FeSi between 4 K and 1173 K determined by time-of-flight neutron powder
773 diffraction. Physics and Chemistry of Minerals, 29, 132 - 139.

774 Wallace, D.C. (1972) Thermodynamics of crystals, 484 p., Wiley, New York.

775 Windsor, C.G. (1981) Pulsed neutron scattering, 432 p., Taylor and Francis, London.

776 Wood, I.G., Knight, K.S., Price, G.D., and Stuart, J.A. (2002) Thermal expansion and atomic
777 displacement parameters of cubic $KMgF_3$ perovskite determined by high-resolution neutron
778 powder diffraction. Journal of Applied Crystallography, 35, 291-295.

779 Wood, I.G., Vočadlo, L., Knight, K.S., Dobson, D.P., Marshall, W.G., Price, G.D., and
780 Brodholt, J.P. (2004) Thermal expansion and crystal structure of cementite, Fe_3C, between 4
781 and 600 K determined by time-of-flight neutron powder diffraction. Journal of Applied
782 Crystallography, 37, 82 - 90.

Zhang, Z., Howard, C.J., Knight, K.S., and Lumpkin, G.R. (2006) Structures of the cation-deficient perovskite $Nd_{0.7}Ti_{0.9}Al_{0.1}O_3$ from high-resolution neutron powder diffraction in combination with group-theoretical analysis. Acta Crystallographica B, 62, 60 – 67.

Zhang, Z., Lumpkin, G.R., Howard, C.J., Knight, K.S., Whittle, K.R., and Osaka, K. (2007) Structures and phase diagram for the system $CaTiO_3$ – $La_{2/3}TiO_3$. Journal of Solid State Chemistry, 180, 1083 – 1092.

Zhao, Y., and Weidner, D.J. (1993) The single crystal elastic moduli of neighborite. Physics and Chemistry of Minerals, 20, 419 – 424.

Zhao, Y., Weidner, D.J., Parise, J.B., and Cox, D.E. (1993a) Thermal expansion and structural distortion of perovskite – data for $NaMgF_3$ perovskite. Part I. Physics of the Earth and Planetary Interiors, 76, 1-16.

Zhao, Y., Weidner, D.J., Parise, J.B., and Cox, D.E. (1993b) Critical phenomena and phase transition of perovskite – data for $NaMgF_3$ perovskite. Part II. Physics of the Earth and Planetary Interiors, 76, 17 - 34.

Zhao, Y., Parise, J.B., Wang, Y., Kusaba, K., Vaughan, M.T., Weidner, D.J., Kikegawa, T., Chen, J, and Shimiomura, O. (1994a) High-pressure crystal chemistry of neighborite, $NaMgF_3$, An angle-dispersive study using monochromatic synchrotron radiation. American Mineralogist, 79, 615 – 621.

Zhao, Y., Weidner, D.J., Ko, J., Leinenweber, K., Liu, X., Li, B., Meng, Y., Pacalo, R.E.G., Vaughan, M.T., Wang, Y., and Yeganeh-Haeri, A. (1994b) Perovskite at high P-T conditions: An in situ synchrotron X ray diffraction study of $NaMgF_3$ perovskite. Journal of Geophysical Research, 99, 2871 – 2885.

Figure Captions

Figure 1. Rietveld fit to the 9 K data collected on neighborite using the high-resolution time-of-flight powder neutron diffractometer HRPD. Upper figure, Rietveld fit to the high-resolution backscattering detector bank, lower figure, the simultaneous fit to the high count-rate, medium resolution 90° detector bank. Observed data are shown as points, the calculated pattern as the full black line, reflection markers are for MgO (upper) and $NaMgF_3$ perovskite (lower). The difference (observed – calculated) is shown as the full black line below the reflection markers for neighborite.

Figure 2. The resolution function for the backscattering detectors of HRPD, shown as the full black line, compared to the C2 diffractometer, shown as the dashed line; both calculated using the 300 K model for the crystal structure of neighborite (Mitchell et al. 2007). The higher resolution time-of-flight instrument is particularly well suited to investigating the subtle structural distortions exhibited by perovskite-structured materials as a function of temperature.

Figure 3. The temperature-dependence of the lattice parameters of neighborite for 9 K ≤ T ≤ 440 K. The lattice parameter *b* (3b) exhibits a narrow region of negative thermal expansion (shown as an inset) that had not been observed in the earlier, lower resolution study (Mitchell et al. 2007). All three data sets have been fitted to a two-term expression described in detail in the text, and shown as the full black lines on the figures. Estimated standard deviations (esds) for all points, in all graphs, are smaller than the size of the plotting symbol used, except for the case of the inset in Fig. 3b, where the esds are comparable in size to the plotting symbol.

Figure 4. The temperature-dependence of the tetragonal (4a) and the orthorhombic shear (4b) spontaneous strains in neighborite between 9 K ≤ T ≤ 440 K. Low temperature data, reported in this paper, are shown as circles, previously unpublished high temperature data are shown as triangles. The low temperature strains have been calculated assuming the aristotype lattice parameter can be approximated by $(V(T)/4)^{1/3}$. Full lines show the predicted behaviour of the spontaneous strains based on critical exponents of 0.25 for the order parameter q_4 (the anti-phase tilt), and 0125 for the order parameter q_2 (the in-phase tilt).

Figure 5. The temperature-dependence of the unit cell volume for neighborite between 9 K ≤ T ≤ 440 K. The full line shows the weighted fit to a two-term Debye internal energy function based on the model of Barron (1998), and described in detail in the text. Esds for the data are smaller than the plotting symbols used.

Figure 6. The temperature-dependence of the thermodynamic Grüneisen parameter for neighborite (black circles) in the temperature interval 313.15 K ≤ T ≤ 443.15 K compared with $CaTiO_3$ perovskite (open circles).

Figure 7. The temperature-variation of the amplitudes of the seven symmetry-adapted basis-vectors consistent with the space group *Pbnm*. The cation displacements are shown in 7a, and 7b, the anion displacements in 7c-7g. The octahedral tilting modes are shown in 7c, and 7d, and form the primary order parameters in the phase transition to the cubic phase; the modes 7e-7g are involved in distortion of the CaF_6 octahedron. The full lines shown in 7a-7b, 7e, and 7g are fits to a function that saturates at low temperatures, as described in the text; the line in 7e is simply a straight line fit to the data. The full line shown in 7c is a fit to critical behaviour with a fixed critical exponent 0.25; that for 6d is an identical fit with fixed exponent of 0.125. The quadratic-quartic coupling between these modes is described in detail in the text.

Figure 8. The temperature-dependences of the five symmetry independent Na – F bonds in the NaF_8 polyhedron. The full lines show the predicted behavior of the bonds based on the parametric fitting of the mode amplitudes. Anion labelling follows Knight (2011a).

Figure 9. The temperature-dependences of the three symmetry independent Mg – F bonds in the MgF_6 octahedron. The full lines show the predicted behavior of the bonds based on the parametric fitting of the mode amplitudes. Anion labelling follows Knight (2011a).

Figure 10. The temperature-dependence of the isotropic atomic displacement parameters for the cations (10a and 10b), and the isotropic, or isotropic equivalent, displacement parameters for the anions (10c and 10d). The full lines on the plots shows fits to these data assuming a Debye density of states function, but permitting the zero point term to be an additional refinable variable (Wood et al. 2002).

Figure 11. The temperature variation of the polyhedral volume strains and their associated thermal expansion coefficients. The NaF_8 polyhedron shows a larger volume strain and greater thermal expansion coefficient than the MgF_6 octahedron at all temperatures above the saturation temperature, reflecting the more open, softer cavity site.

Figure 12. The linear-quadratic coupling of the anti-phase tilt to the in-phase tilt in neighborite. The full line shows a simple straight line fit to all the data, the dashed line shows a fit to the data for a maximum anti-phase displacement of 0.35 Å that is constrained to pass through the origin.

874 **Table 1.** Structural parameters for $NaMgF_3$ at 9 K

Lattice parameters (Å)	*a*	5.32517(2)
	b	5.47795(2)
	c	7.62732(3)
Unit cell volume ($Å^3$)		222.497(1)
Na	*x*	-0.0125(2)
	y	0.5497(2)
	$100u_{iso}$ ($Å^2$)	0.498(25)
Mg	$100u_{iso}$ ($Å^2$)	0.045(17)
F1	*x*	0.0931(1)
	y	-0.0301(1)
	$100u_{iso}$ ($Å^2$)	0.205(18)
F2	*x*	0.29816(9)
	y	0.20414(9)
	z	-0.04857(6)
	$100u_{iso}$ ($Å^2$)	0.258(14)
Bond lengths (Å)		
Mg – F1(1)	×2	1.9771(2)
Mg – F2(1)	×2	1.9771(4)
Mg – F2(4) i	×2	1.9797(5)
Na – F1(1') ii		2.3697(12)
Na – F1(3') iii		2.2756(14)
Na – F2(8) iii	×2	2.6841(14)
Na – F2(3) iv	×2	2.3045(10)
Na – F2(7) v	×2	2.5481(11)
Polyhedral volumes ($Å^3$)	MgF_6	10.311(3)
	NaF_8	24.358(11)
Rp[a]		0.042
Rwp[a]		0.037

875 Space group: *Pbnm*. Na, F1: 4*c* *x*, *y*, 1/4, Mg: 4*a* 0, 0, 0.

876 [a] 6348 observations and 29 variables (joint refinement of $NaMgF_3$ and MgO)

877 i) *x*-½, ½-*y*,-*z*; ii) *x*, 1+*y*, *z*; iii) ½-*x*, ½+*y*, *z*; iv) -½+*x*, ½-*y*, ½+*z*; v) –*x*, 1-*y*, ½+*z*

878

879 **Table 2.** Refined fitting parameters for the temperature-dependence of the lattice parameters

880 of neighborite in the temperature interval 9 K ≤ T ≤ 440 K.

axis	l_0/Å	k_1/Å	θ_1/K	k_2/Å	θ_2/K	r^2
a	5.32522(1)	0.0560(6)	742(15)	0.0316(7)	229(2)	0.999997
b	5.47799(2)	0.0472(3)	568(5)	$-2.4(1.4) \times 10^{-4}$	41(21)	0.999947
c	7.62736(1)	0.0298(8)	217(3)	0.0691(5)	706(12)	0.999896

881

882

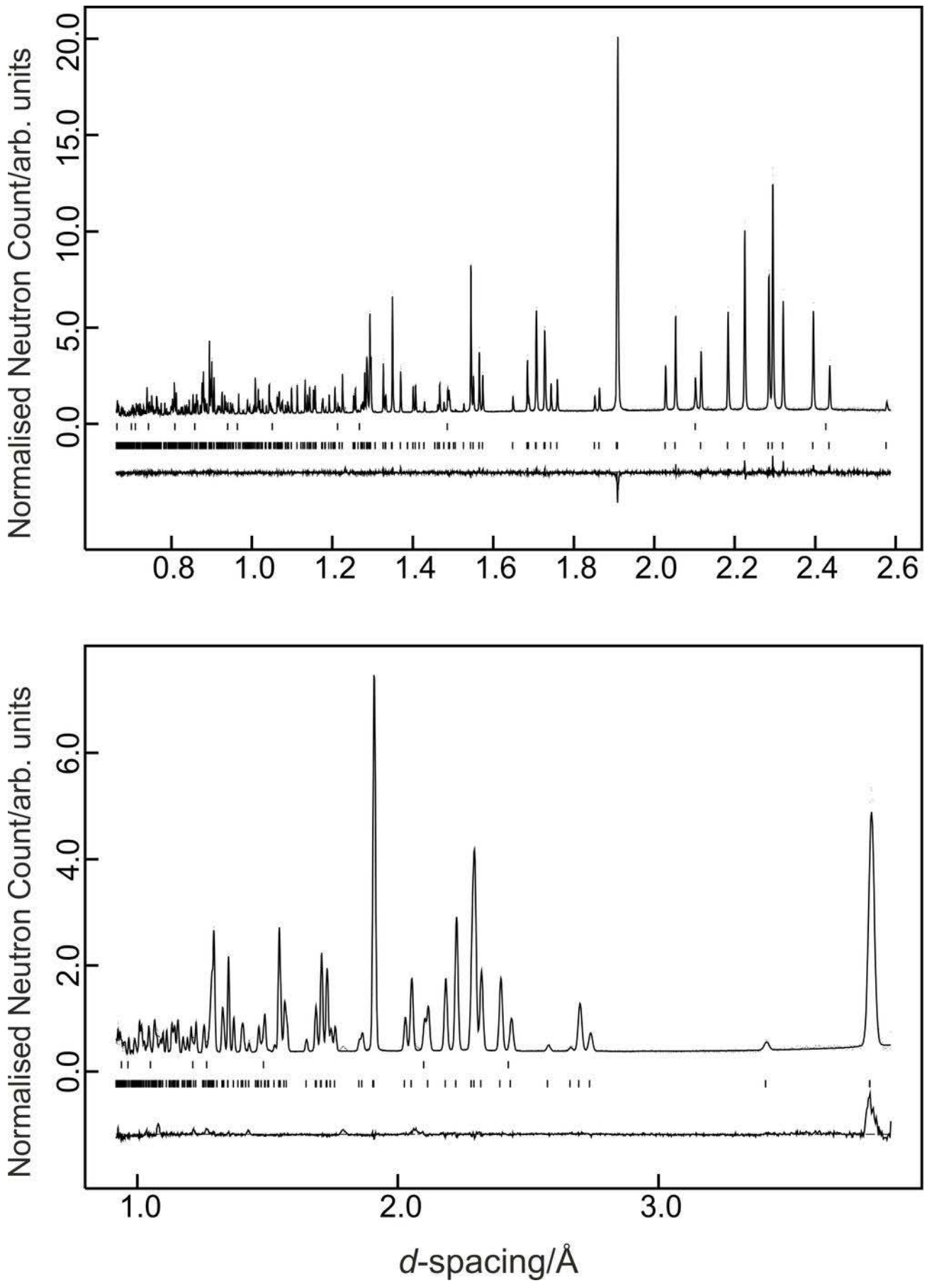
Normalised Neutron Count/arb. units
0.0
5.0
10.0
15.0
20.0
0.8
1.0
1.2
1.4
1.6
1.8
2.0
2.2
2.4
2.6
Normalised Neutron Count/arb. units
0.0
2.0
4.0
6.0
1.0
2.0
3.0
d-spacing/Å

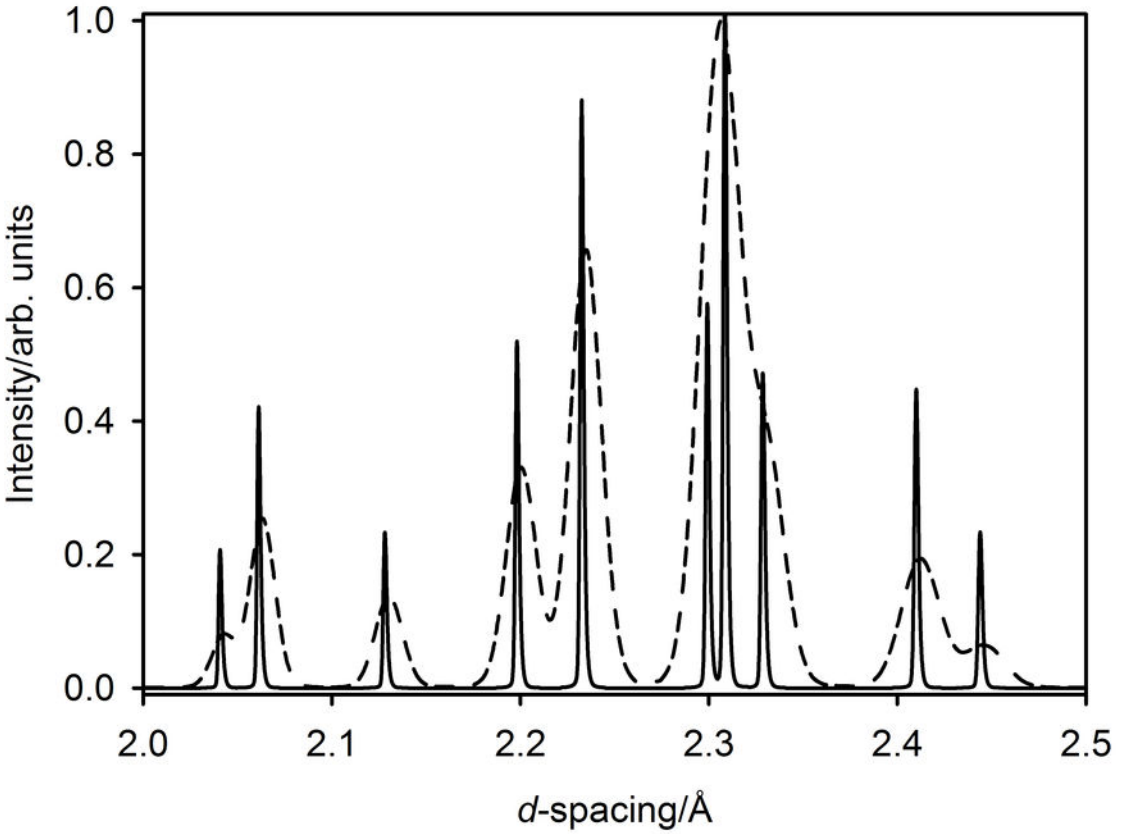
1.0
0.8
0.6
0.4
0.2
0.0
Intensity/arb. units
2.0
2.1
2.2
2.3
2.4
2.5
d-spacing/Å

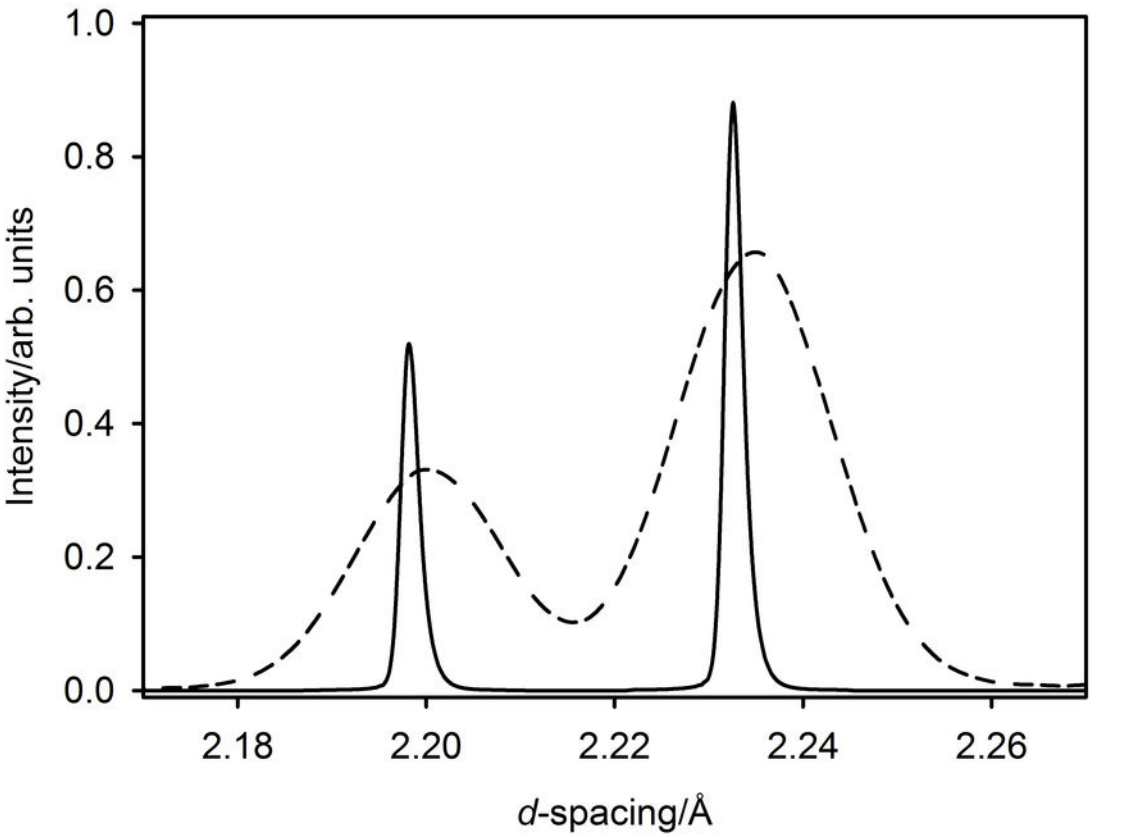
1.0
0.8
0.6
0.4
0.2
0.0
Intensity/arb. units
2.18
2.20
2.22
2.24
2.26
d-spacing/Å

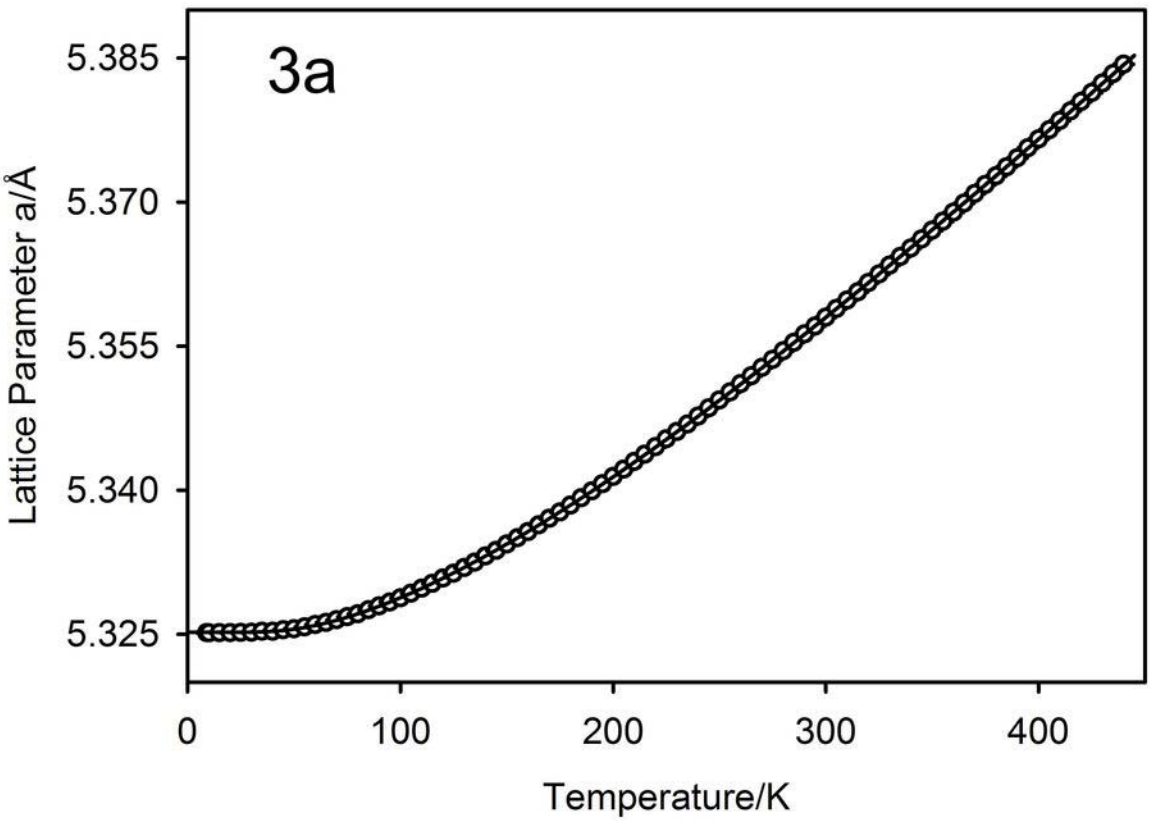
3a
5.385
5.370
5.355
5.340
5.325
Lattice Parameter a/Å
0
100
200
300
400
Temperature/K

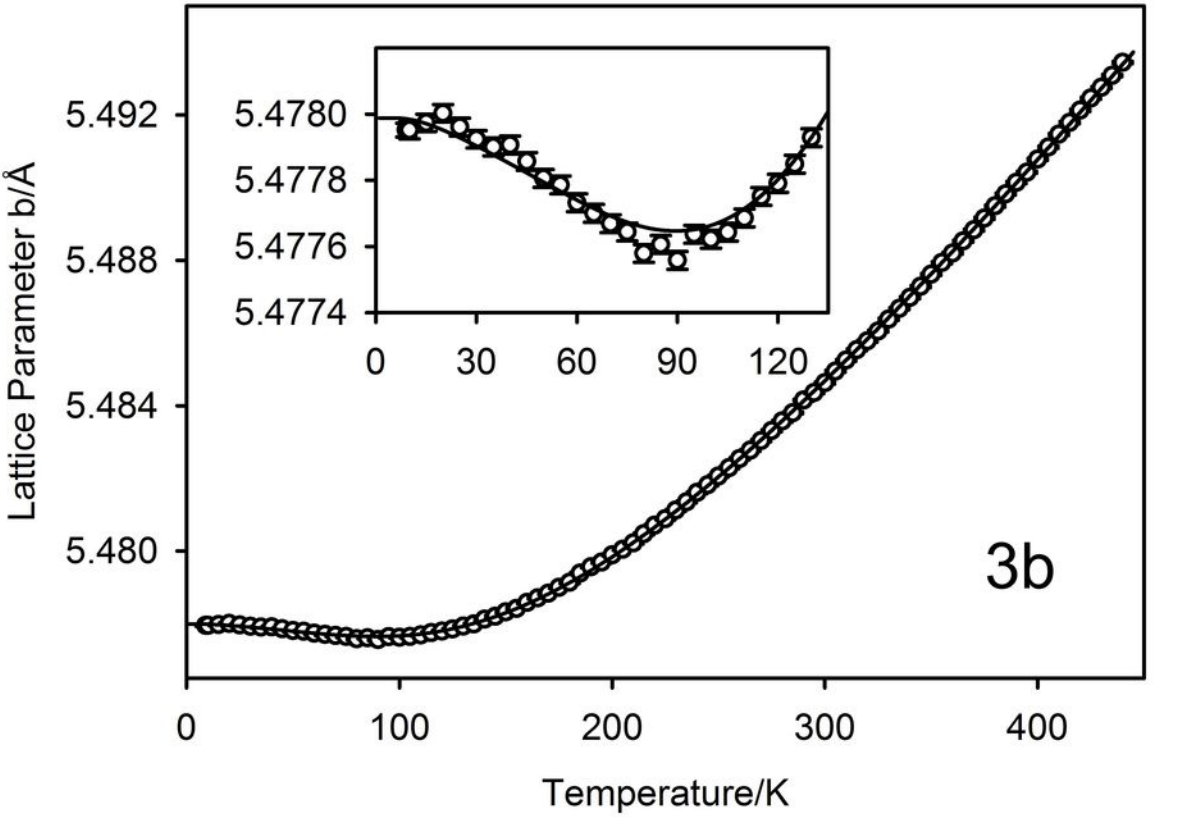
Lattice Parameter b/Å
5.492
5.488
5.484
5.480
0
100
200
300
400
Temperature/K
5.4780
5.4778
5.4776
5.4774
0
30
60
90
120
3b

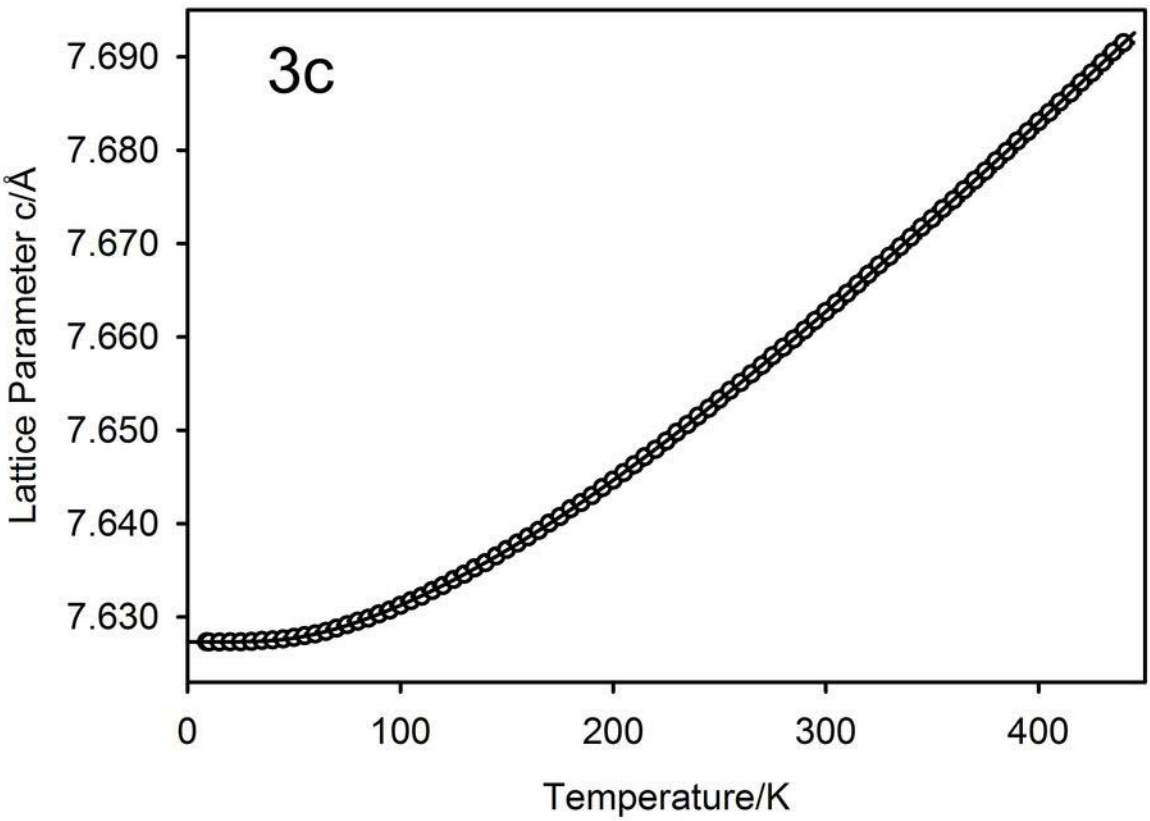
3c
Lattice Parameter c/Å
7.690
7.680
7.670
7.660
7.650
7.640
7.630
0
100
200
300
400
Temperature/K

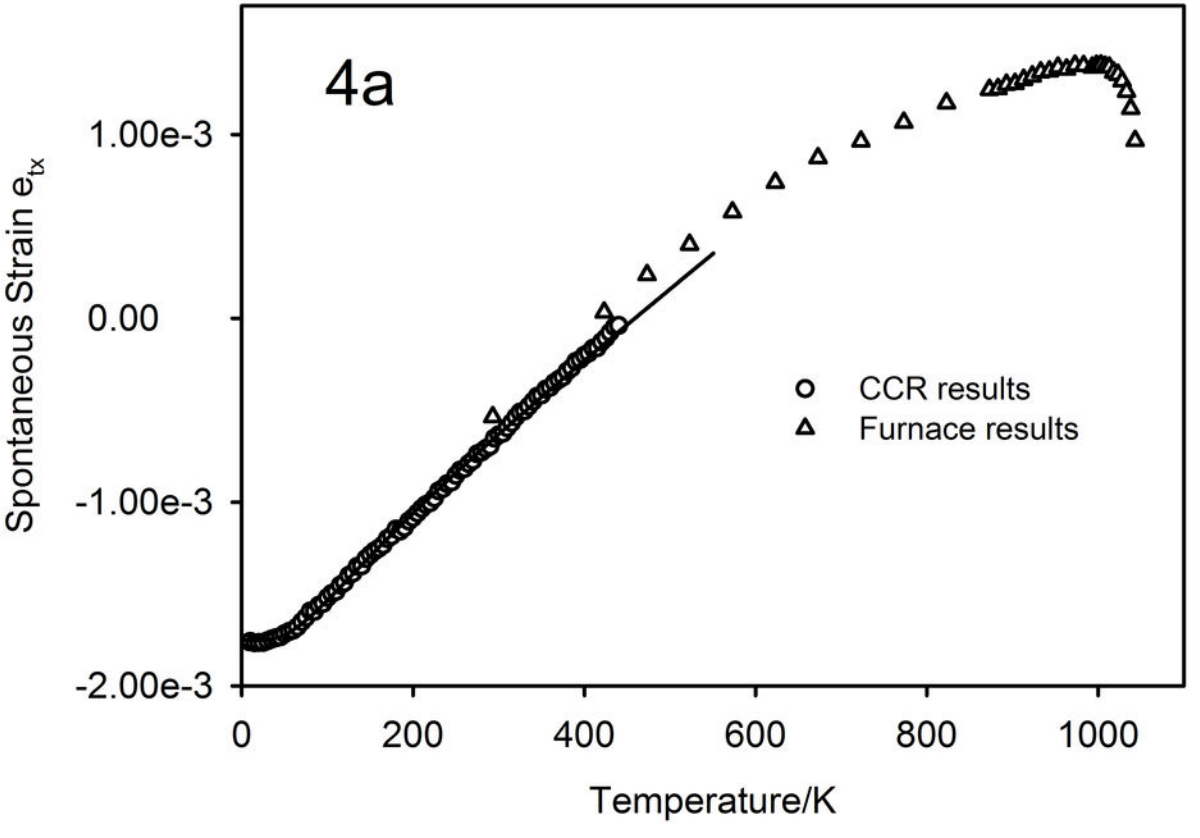
4a
1.00e-3
0.00
-1.00e-3
-2.00e-3
Spontaneous Strain e_{tx}
0
200
400
600
800
1000
Temperature/K
CCR results
Furnace results

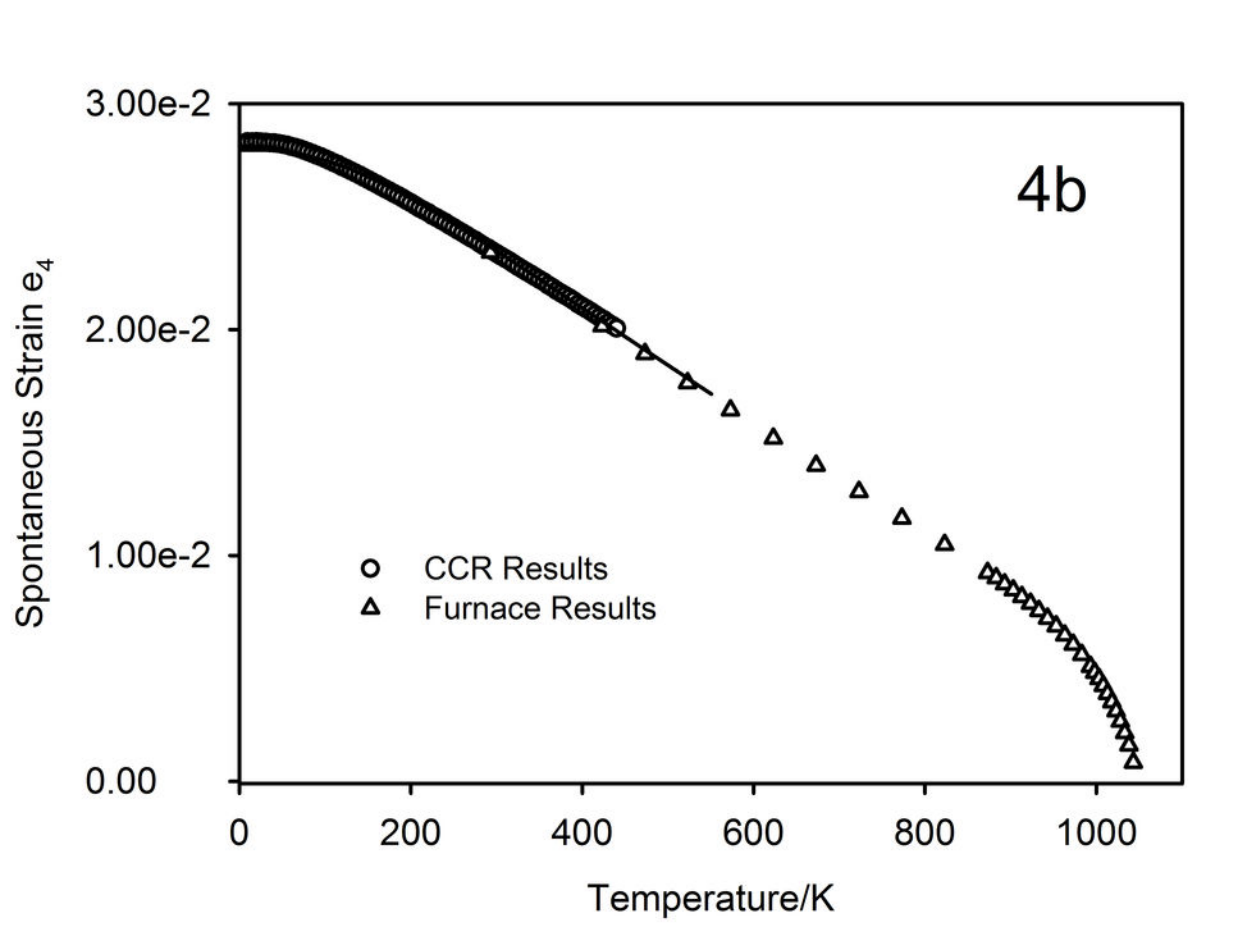
4b
3.00e-2
2.00e-2
1.00e-2
0.00
Spontaneous Strain e_4
0
200
400
600
800
1000
Temperature/K
CCR Results
Furnace Results

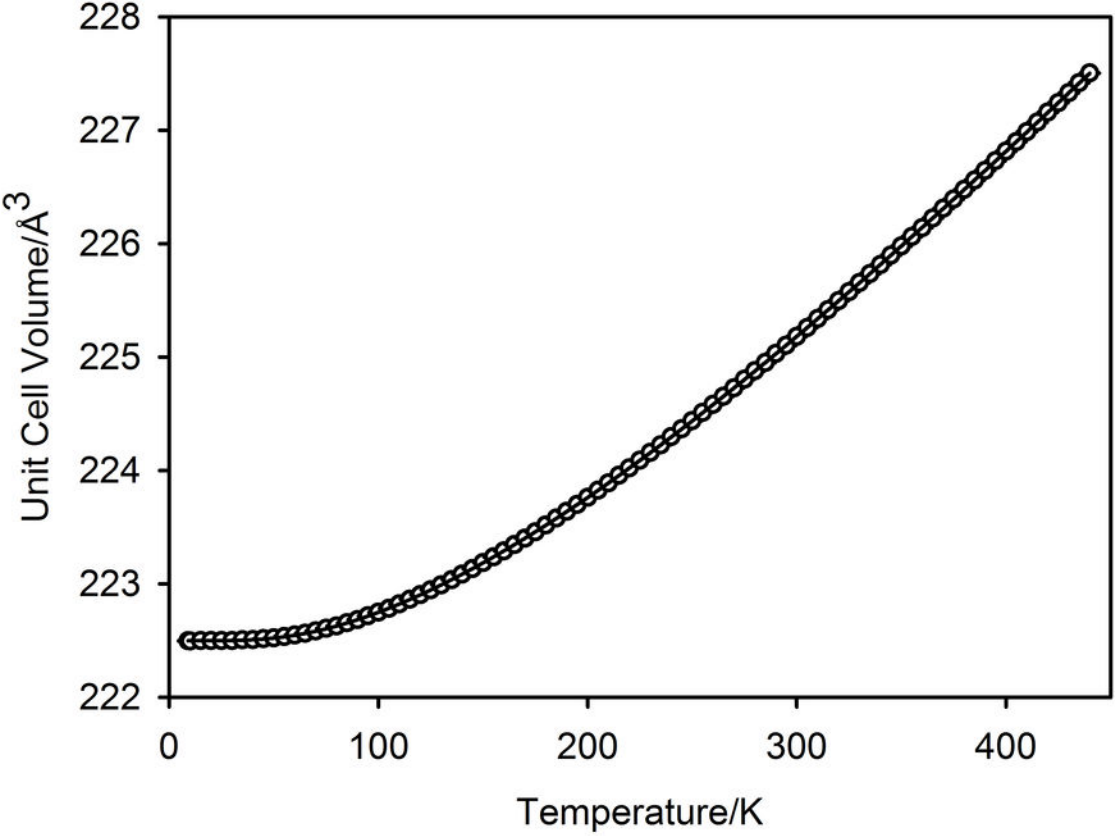
228
227
226
225
224
223
222
Unit Cell Volume/Å3
0
100
200
300
400
Temperature/K

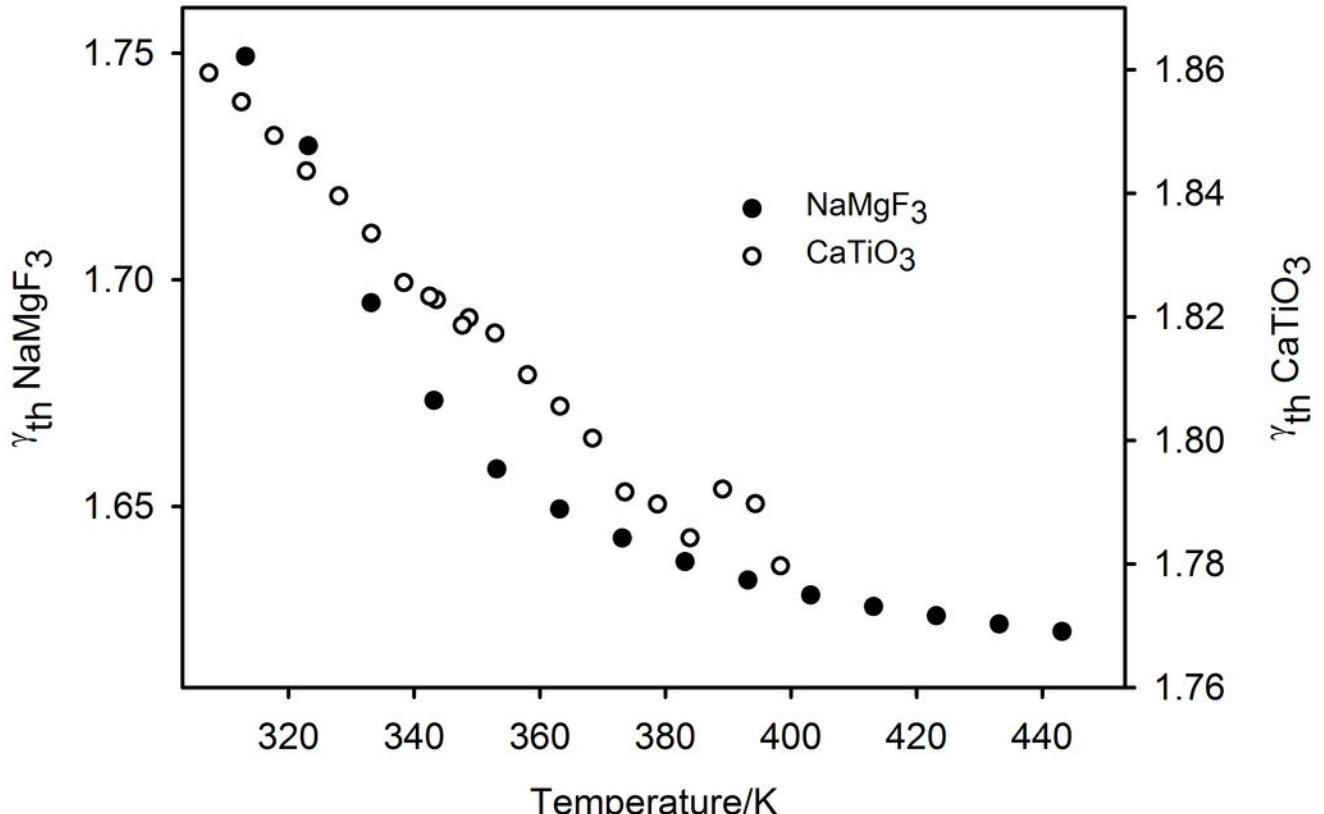
1.75
1.70
1.65
1.86
1.84
1.82
1.80
1.78
1.76
320
340
360
380
400
420
440
Temperature/K
γ_{th} NaMgF$_3$
γ_{th} CaTiO$_3$
NaMgF$_3$
CaTiO$_3$

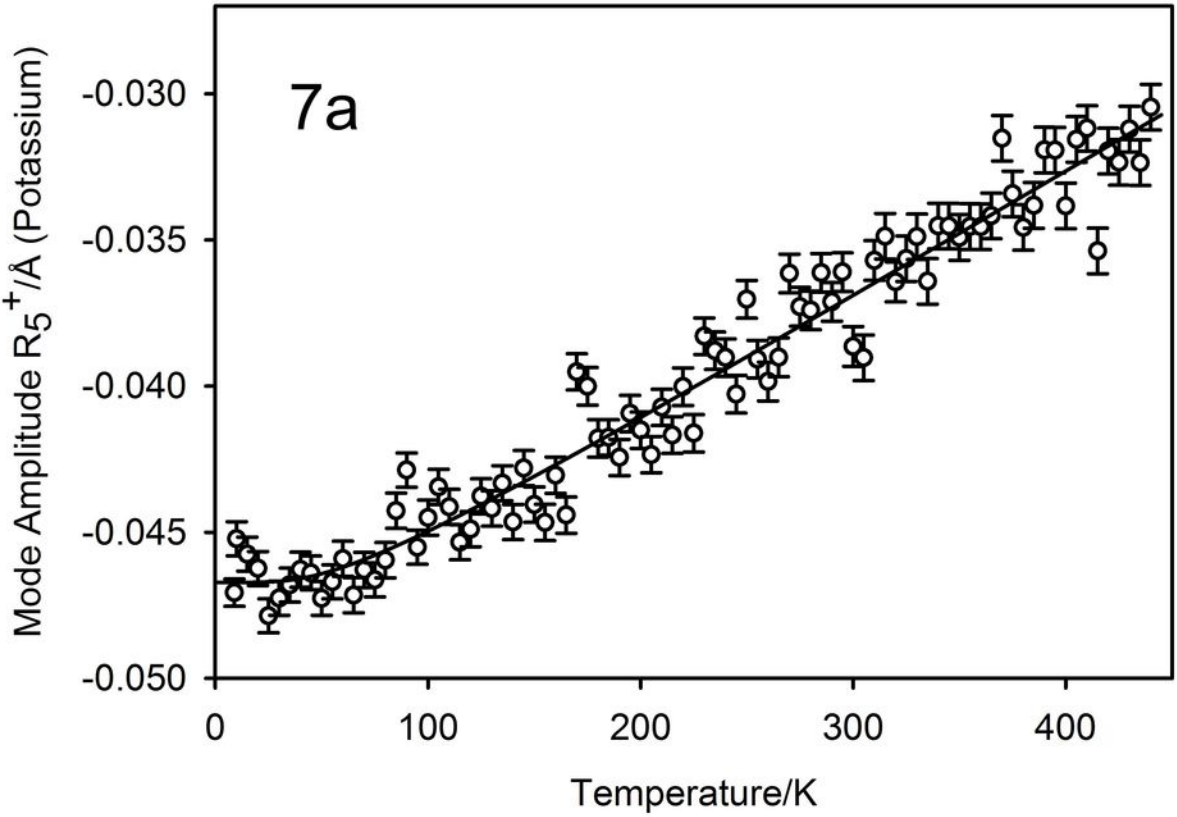
7a
-0.030
-0.035
-0.040
-0.045
-0.050
Mode Amplitude R_5^+/Å (Potassium)
0
100
200
300
400
Temperature/K

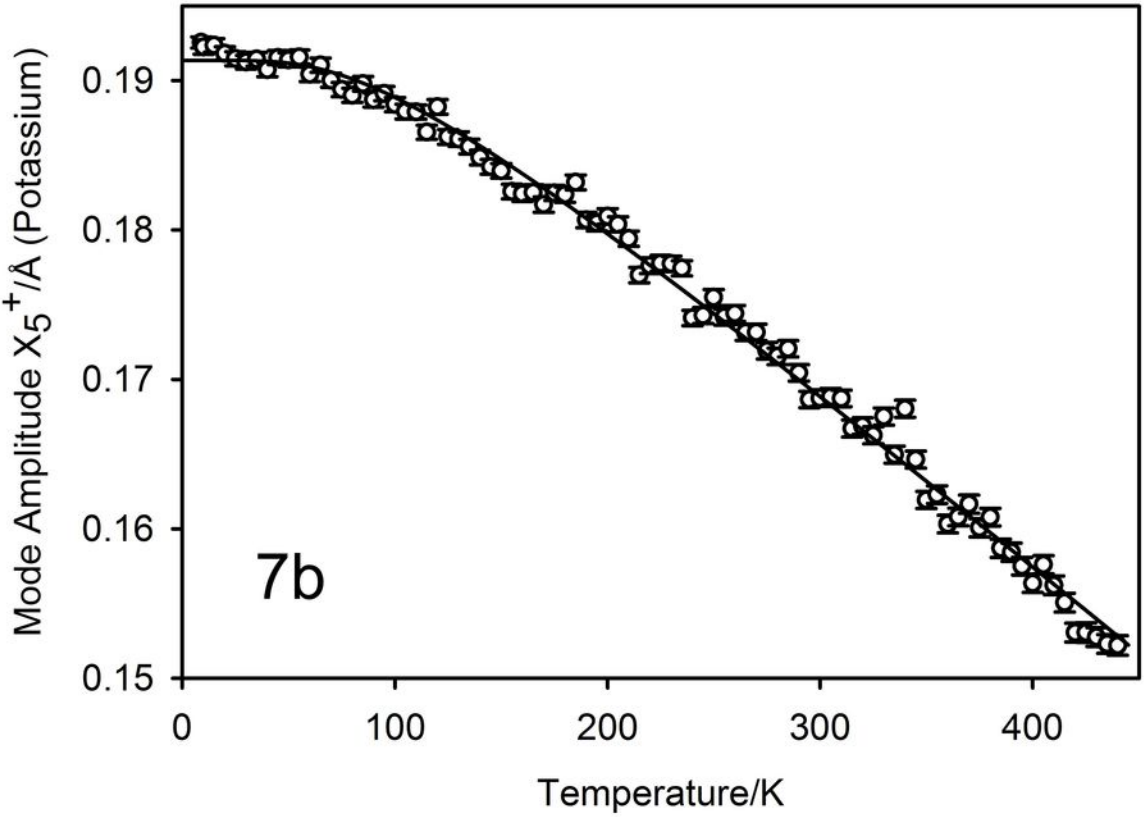
Mode Amplitude X_5^+/Å (Potassium)
0.19
0.18
0.17
0.16
0.15
7b
0
100
200
300
400
Temperature/K

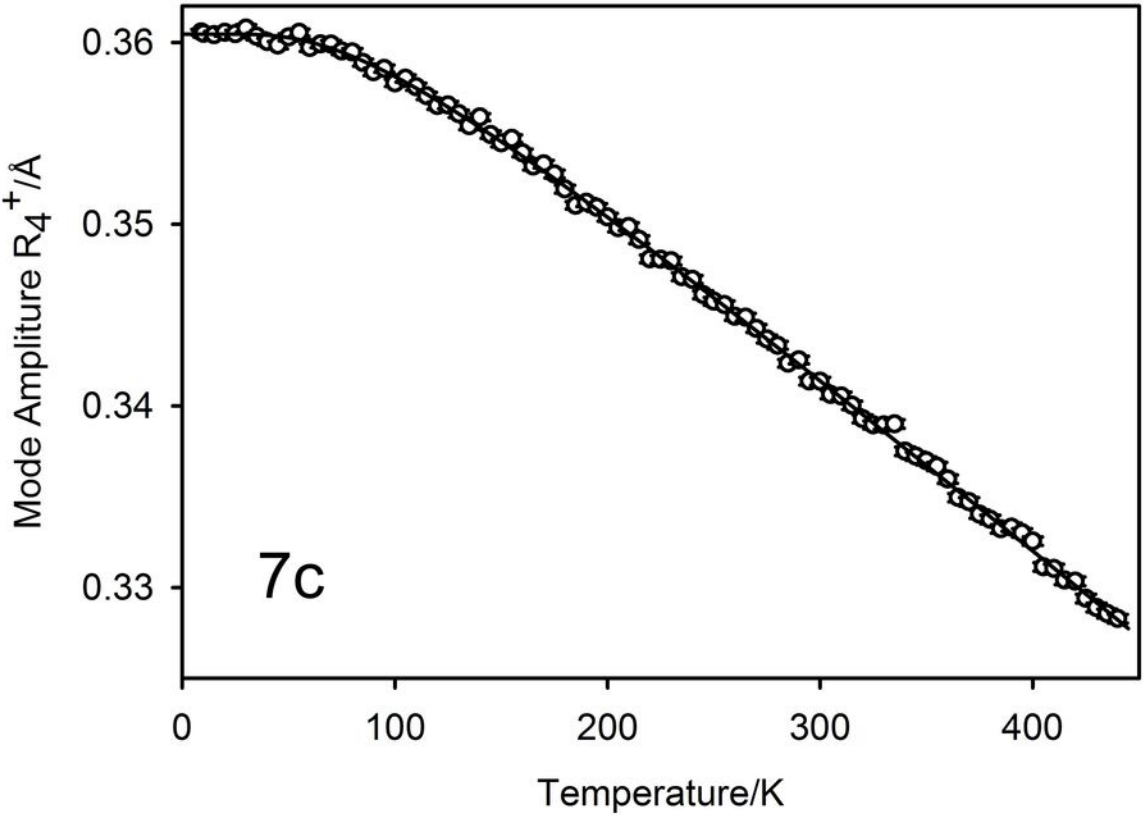
0.36
0.35
0.34
0.33
Mode Ampliture R_4^+/Å
7c
0
100
200
300
400
Temperature/K

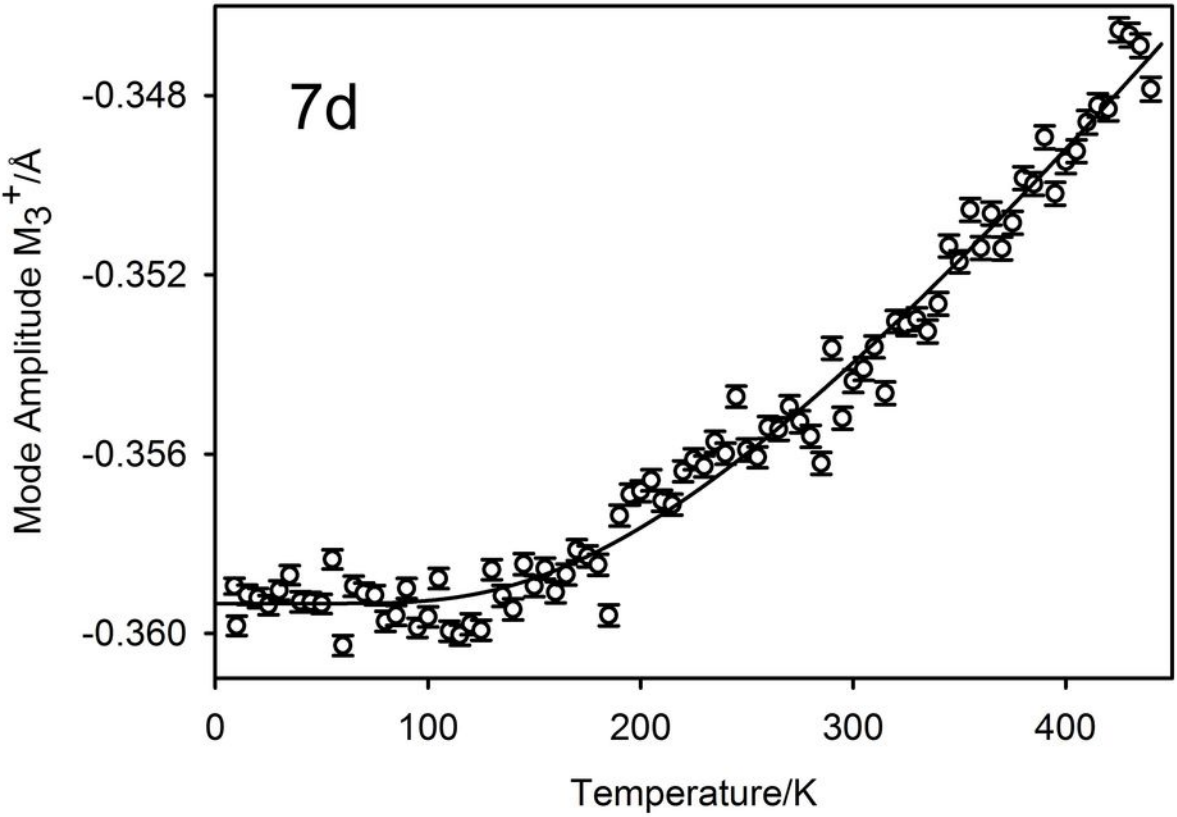
7d
-0.348
-0.352
-0.356
-0.360
Mode Amplitude M_3^+/Å
0
100
200
300
400
Temperature/K

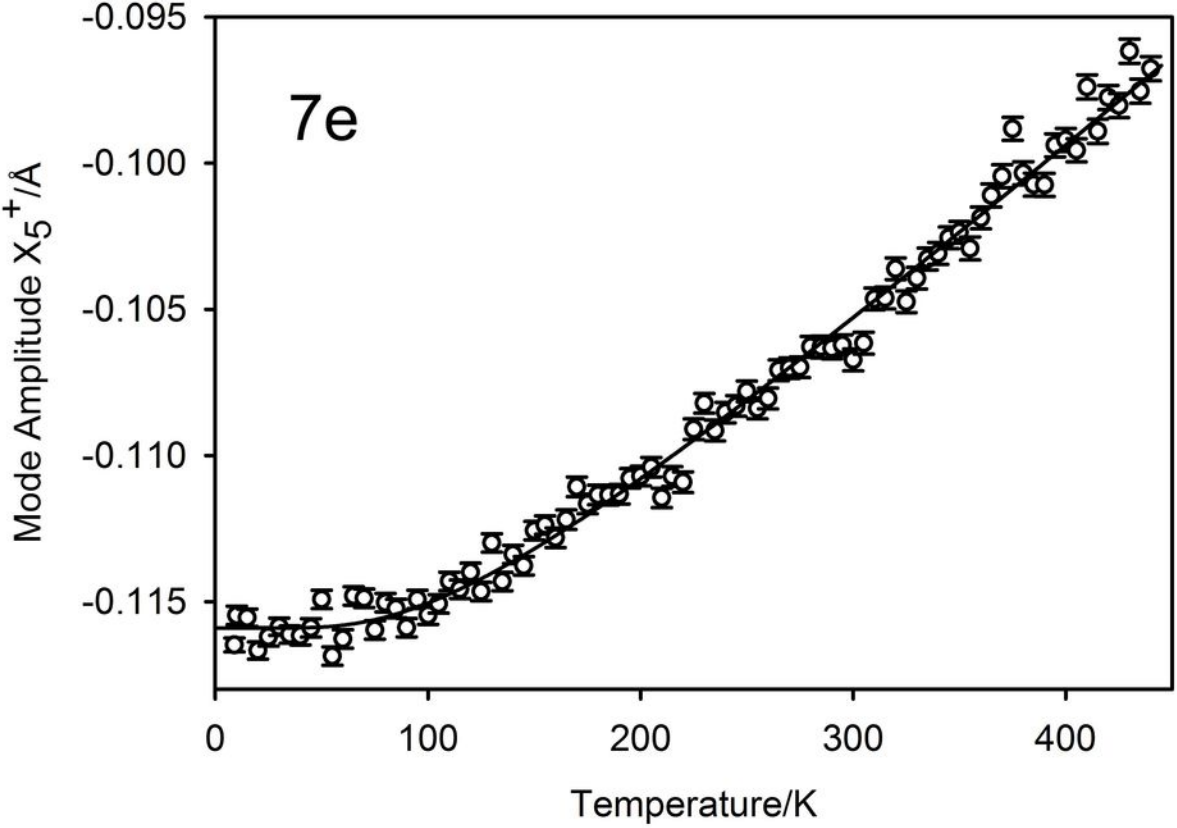
7e
-0.095
-0.100
-0.105
-0.110
-0.115
Mode Amplitude X_5^+/Å
0
100
200
300
400
Temperature/K

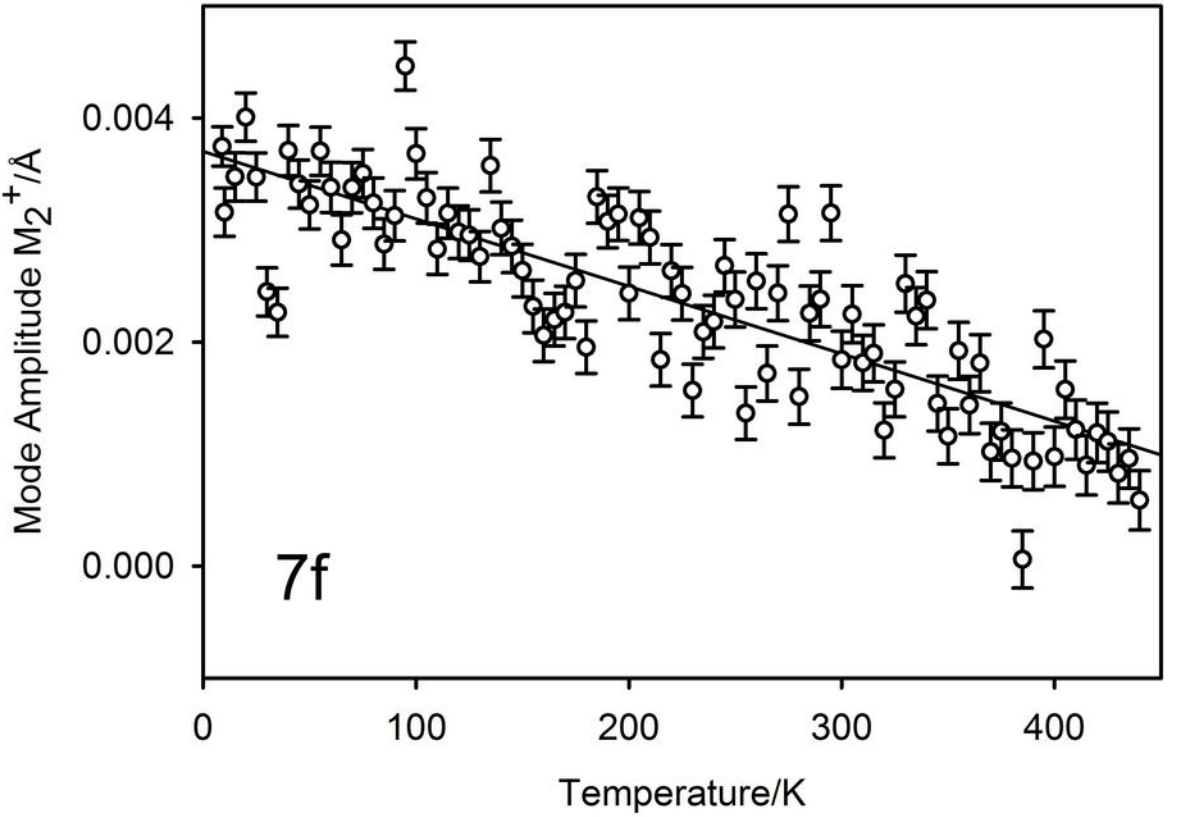
0.004
0.002
0.000
Mode Amplitude M_2^+/Å
7f
0
100
200
300
400
Temperature/K

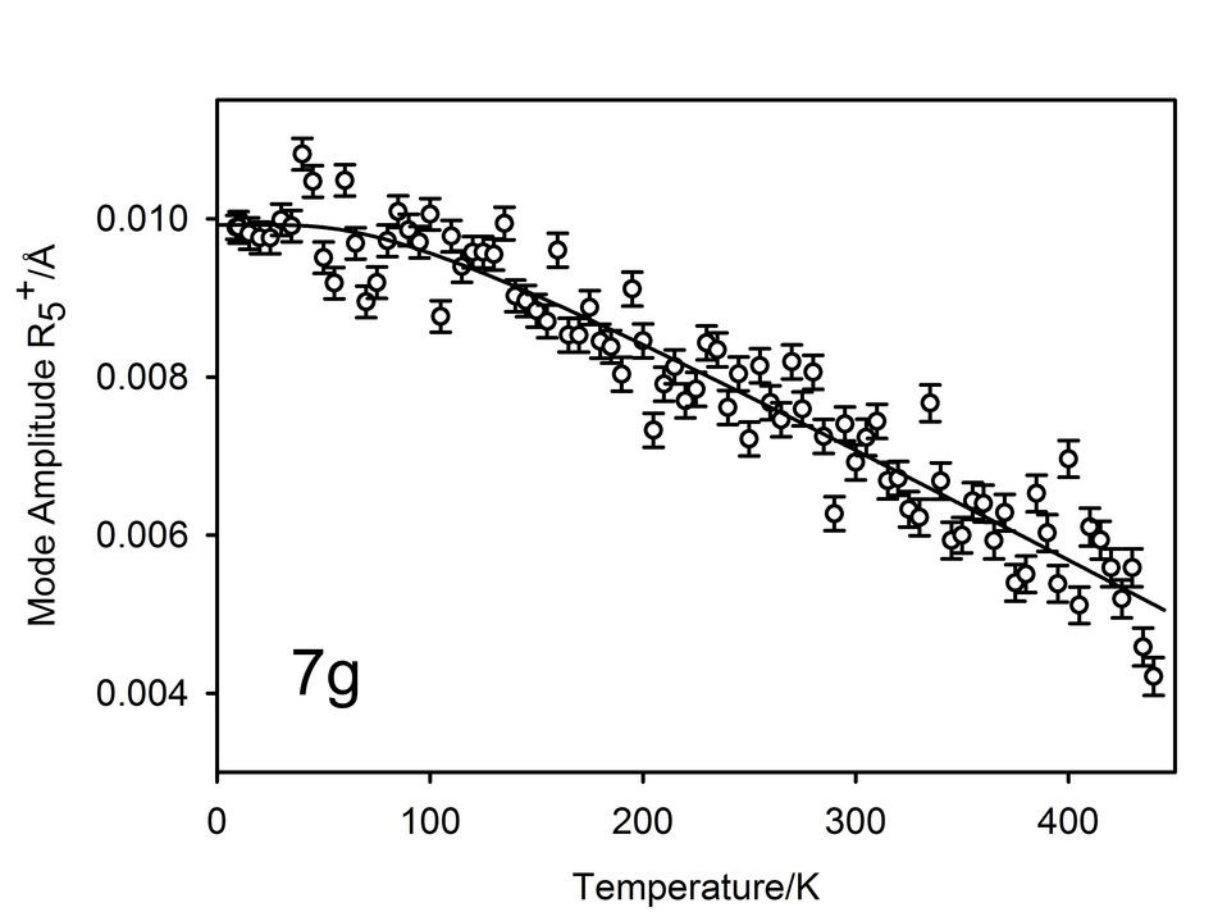
0.010
0.008
0.006
0.004
Mode Amplitude R_5^+/Å
7g
0
100
200
300
400
Temperature/K

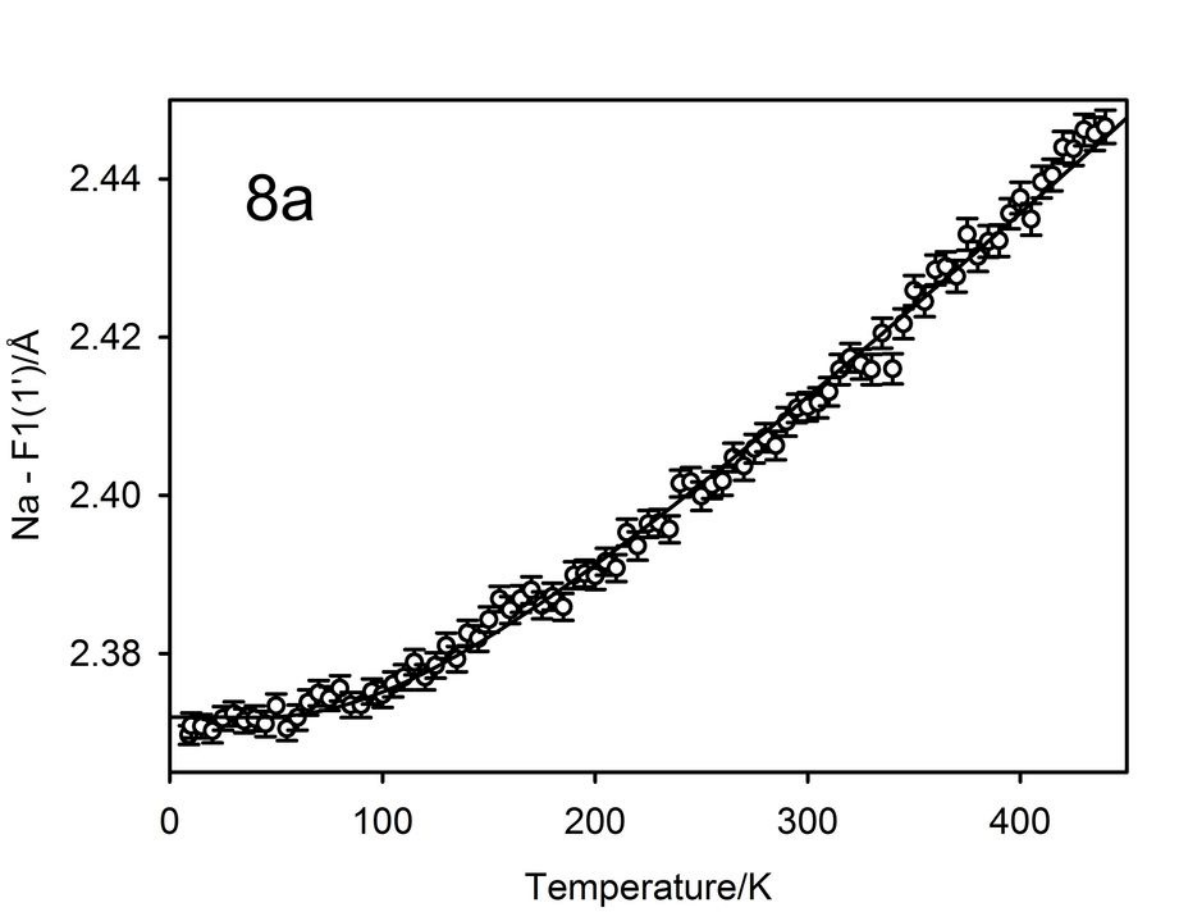
8a
2.44
2.42
2.40
2.38
Na - F1(1')/Å
0
100
200
300
400
Temperature/K

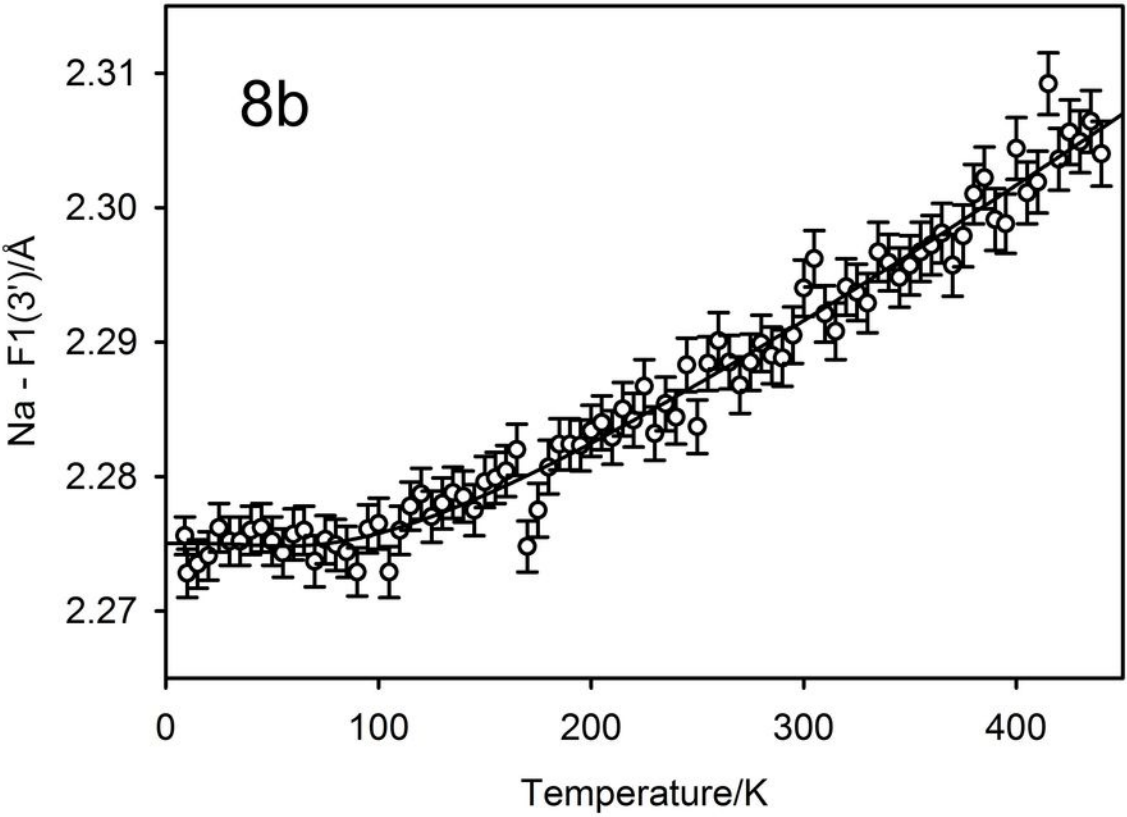
8b
2.31
2.30
2.29
2.28
2.27
Na - F1(3')/Å
0
100
200
300
400
Temperature/K

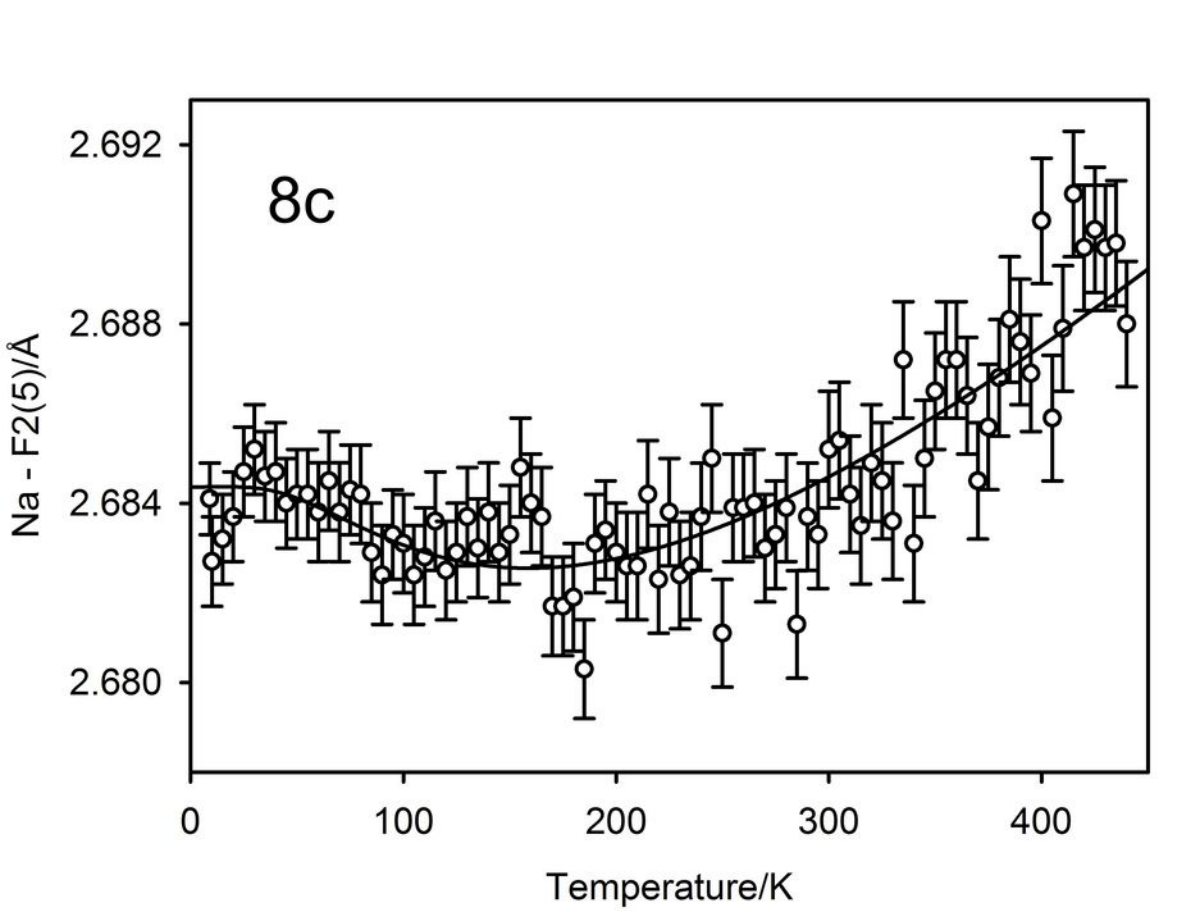
8c
2.692
2.688
2.684
2.680
Na - F2(5)/Å
0
100
200
300
400
Temperature/K

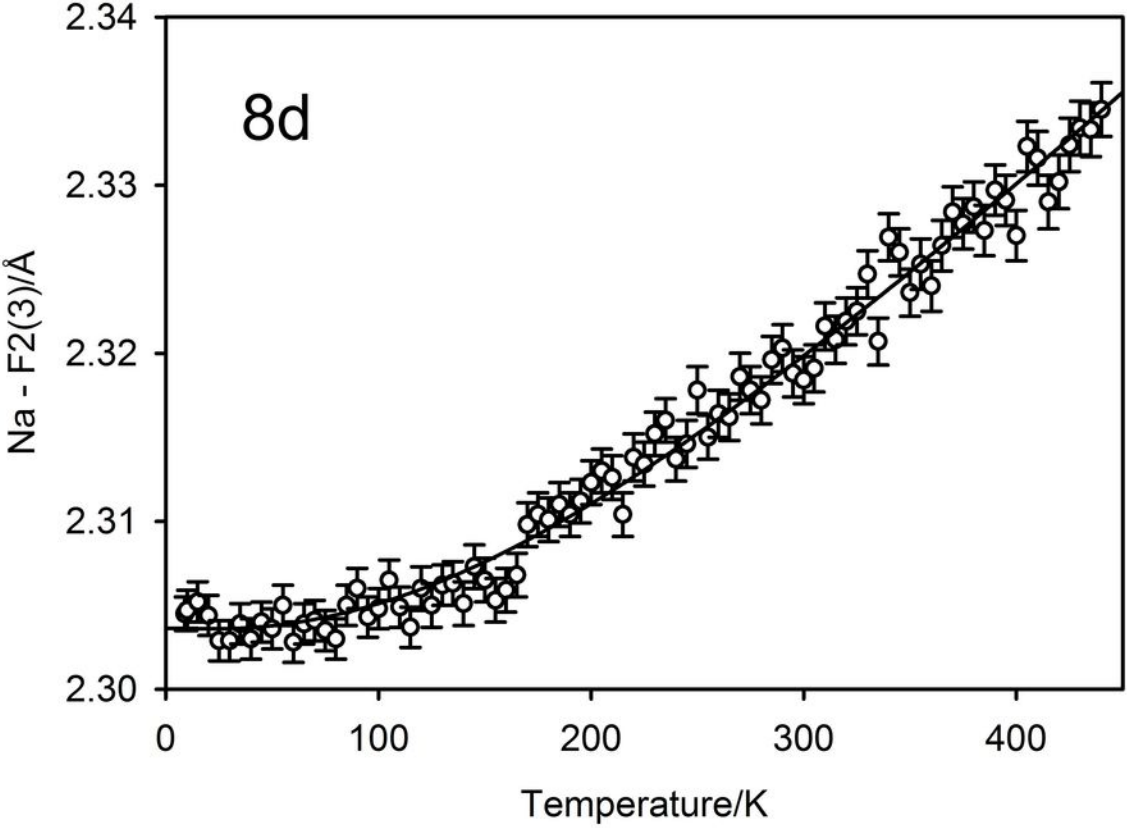
8d
2.34
2.33
2.32
2.31
2.30
Na - F2(3)/Å
0
100
200
300
400
Temperature/K

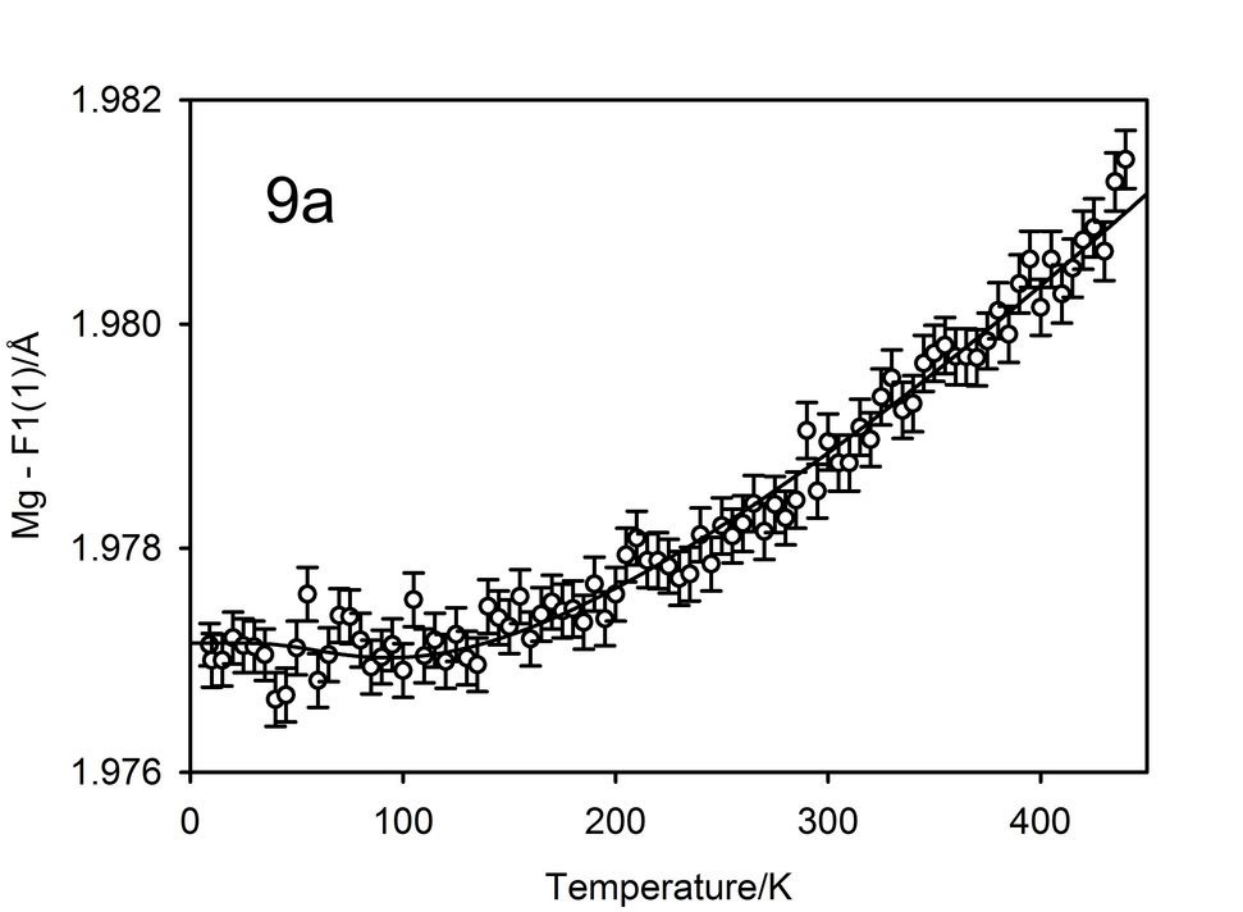
9a
1.982
1.980
1.978
1.976
Mg - F1(1)/Å
0
100
200
300
400
Temperature/K

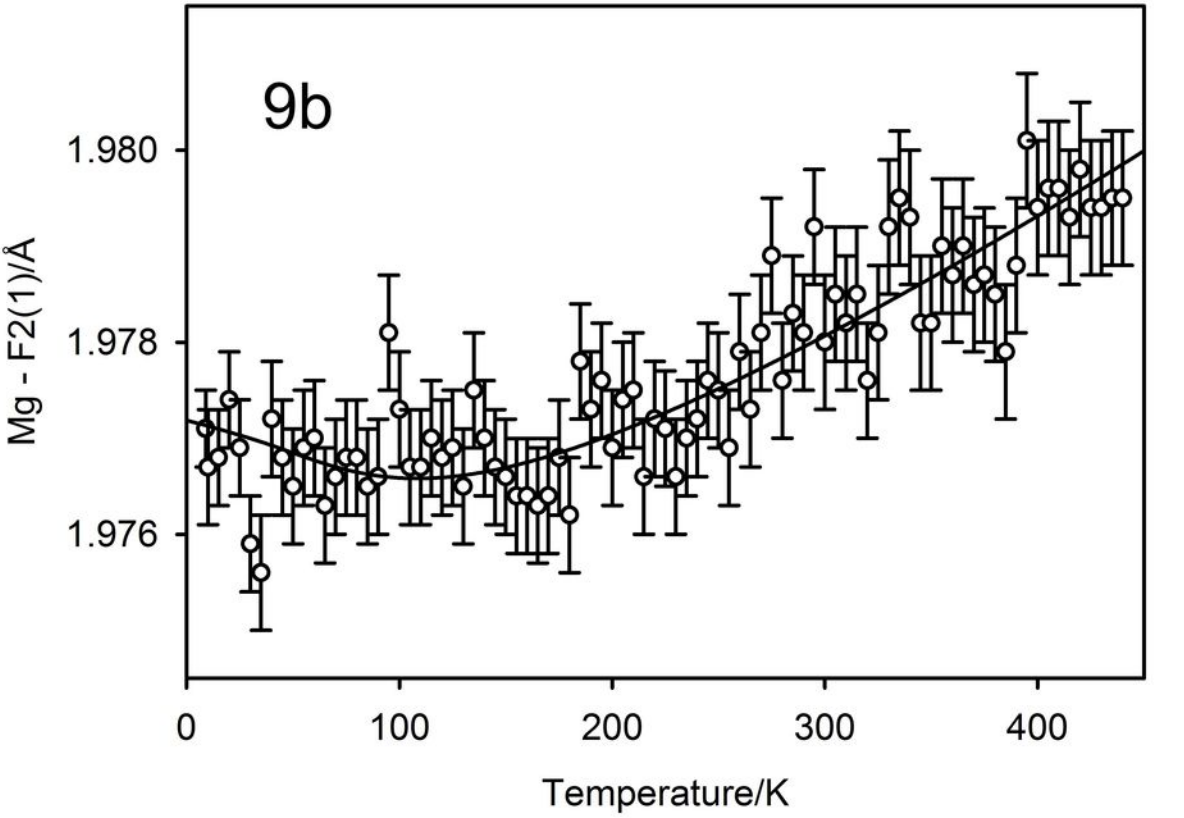
9b
1.980
1.978
1.976
Mg - F2(1)/Å
0
100
200
300
400
Temperature/K

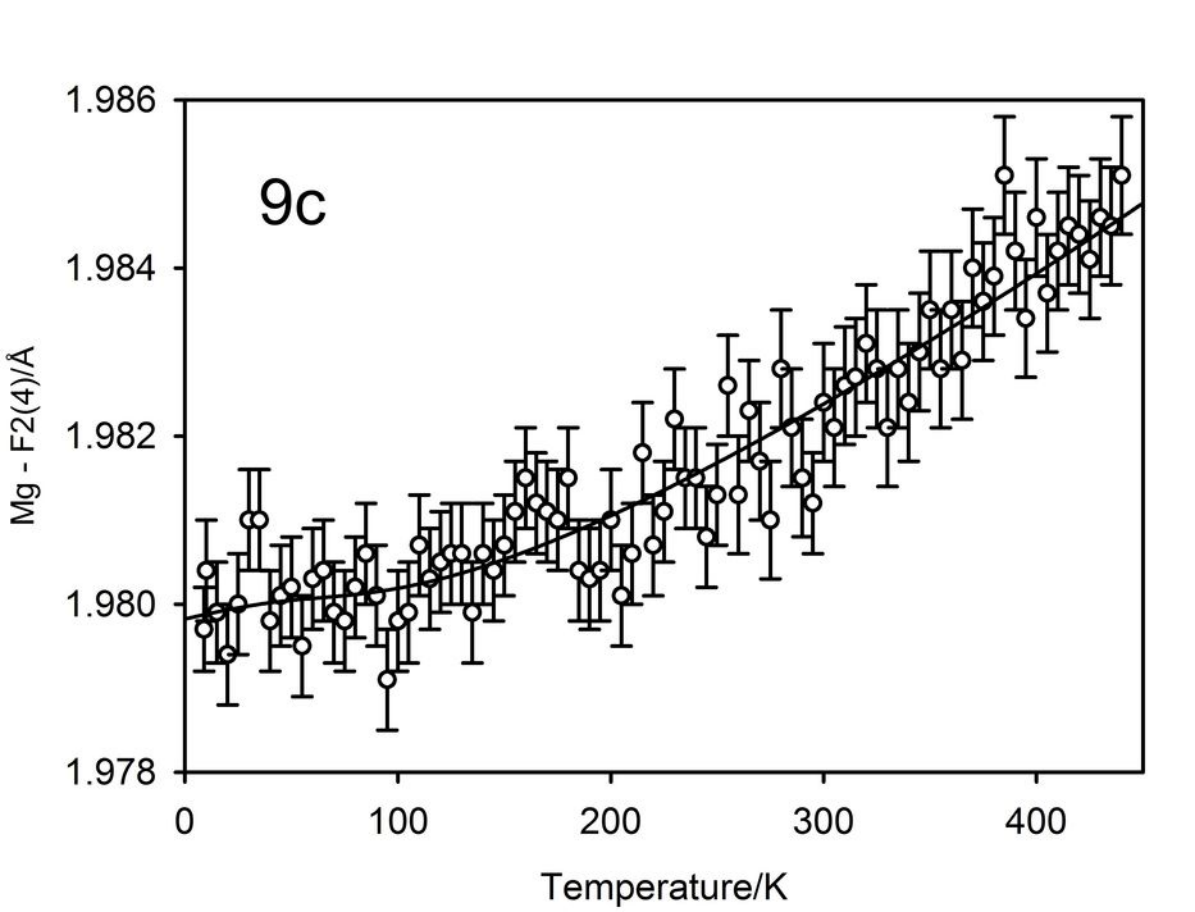
9c
1.986
1.984
1.982
1.980
1.978
Mg - F2(4)/Å
0
100
200
300
400
Temperature/K

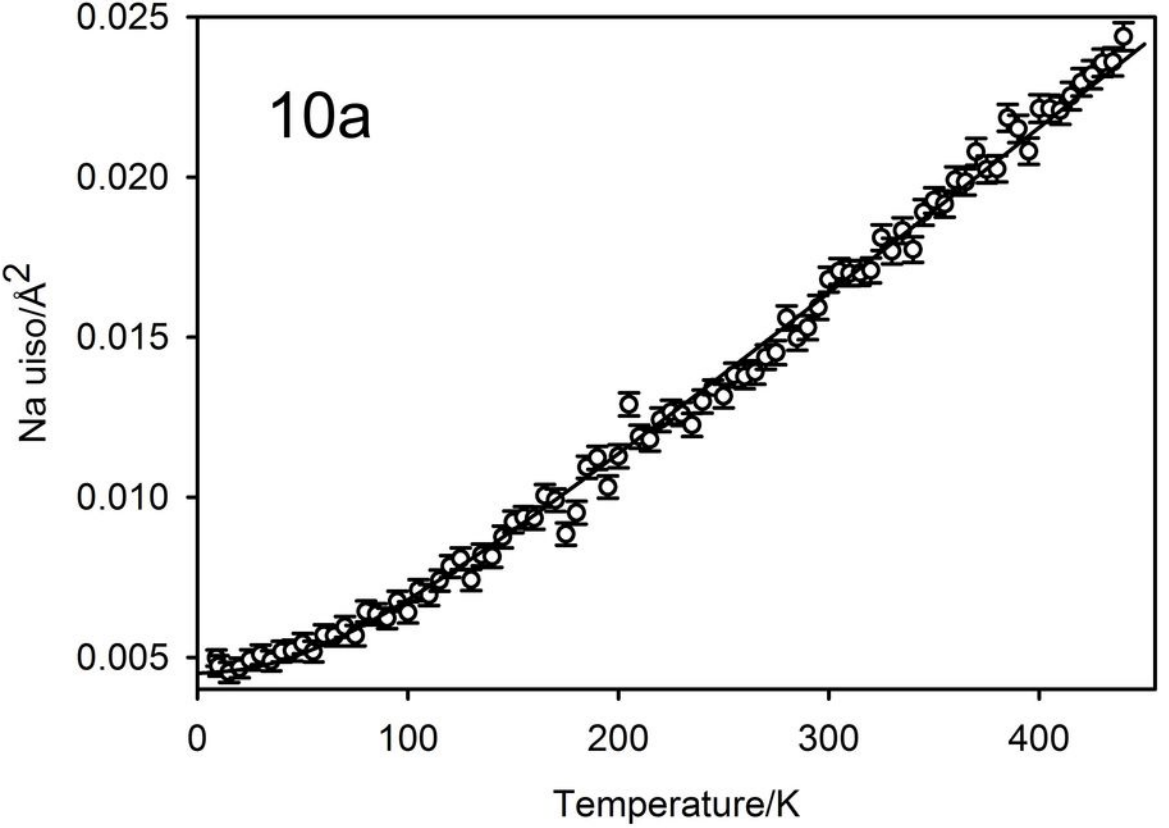
10a
0.025
0.020
0.015
0.010
0.005
Na uiso/Å2
0
100
200
300
400
Temperature/K

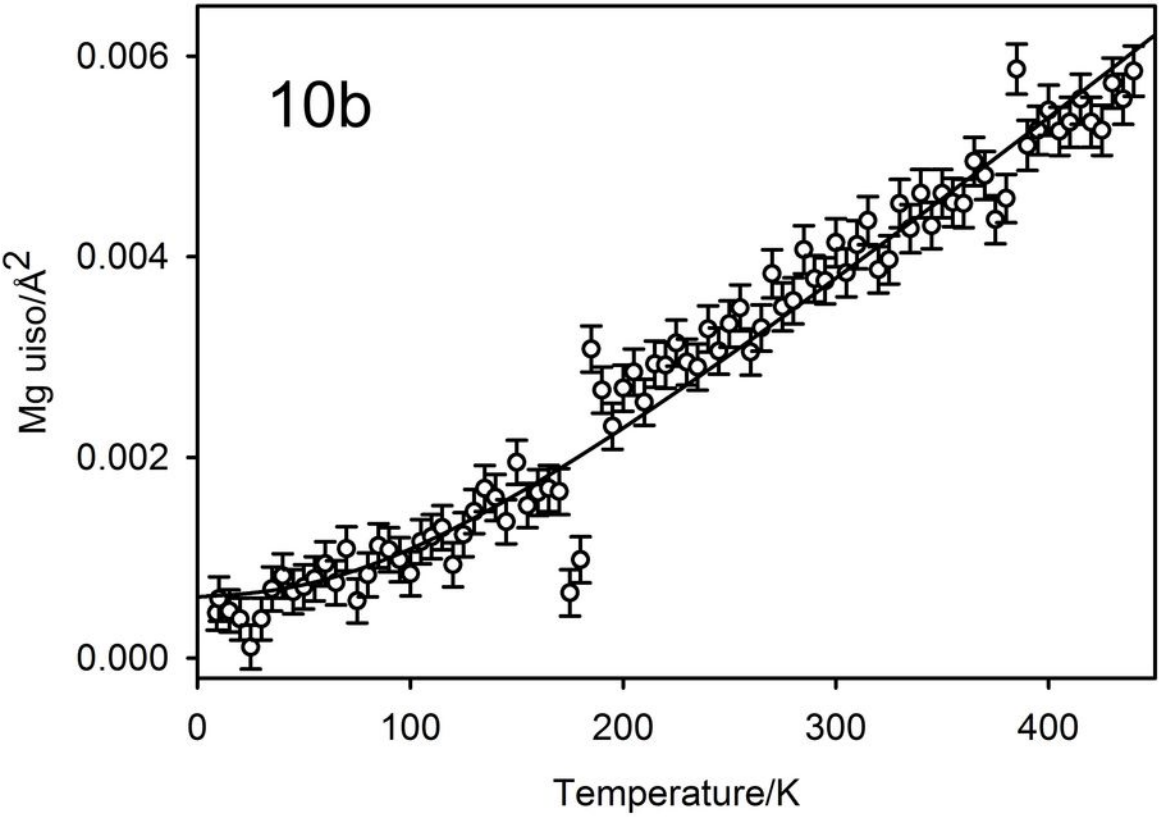
10b
0.006
0.004
0.002
0.000
Mg uiso/Å2
0
100
200
300
400
Temperature/K

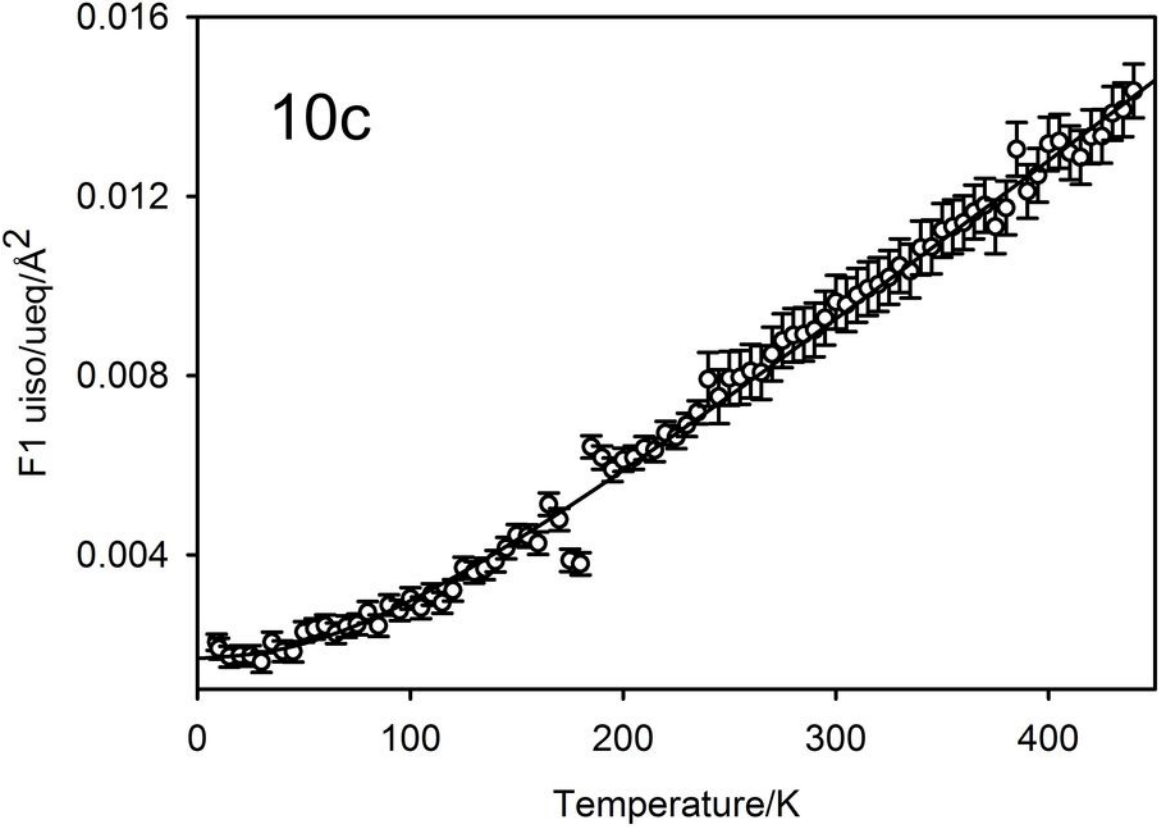
10c
0.016
0.012
0.008
0.004
F1 uiso/ueq/Å2
0
100
200
300
400
Temperature/K

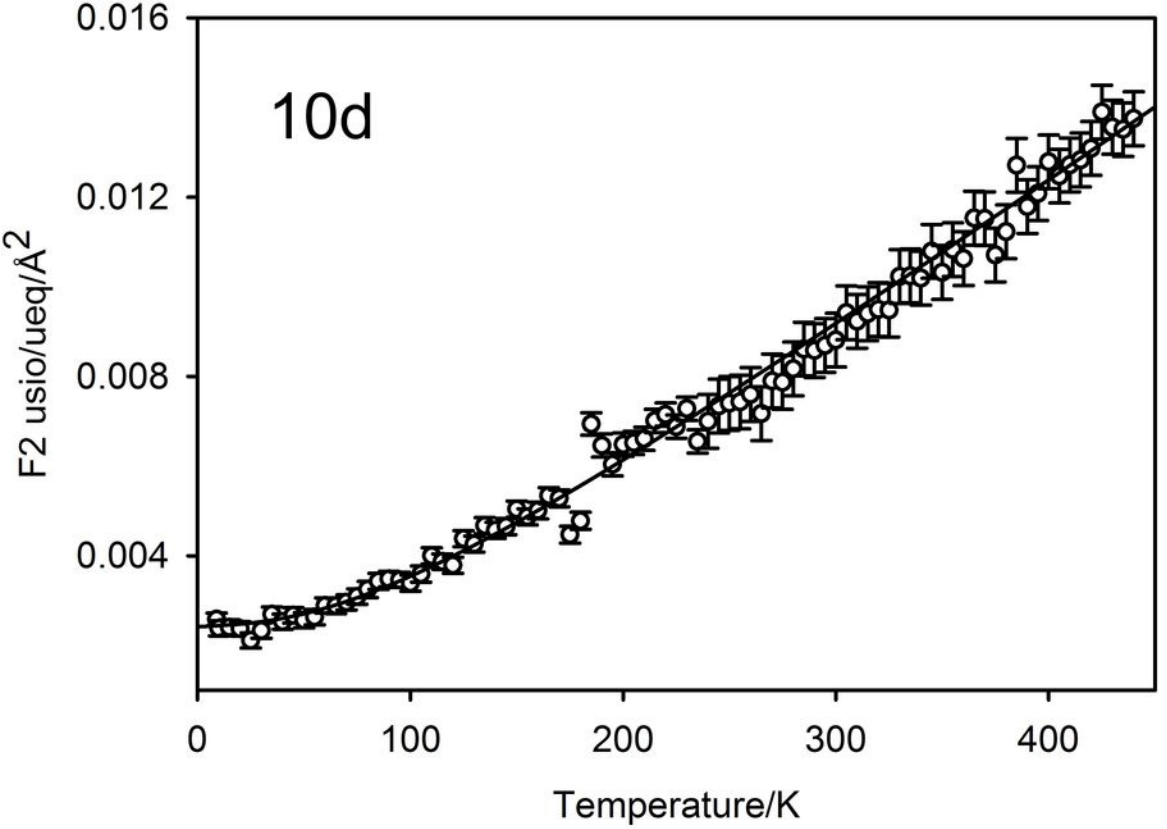
10d
0.016
0.012
0.008
0.004
F2 usio/ueq/Å2
0
100
200
300
400
Temperature/K

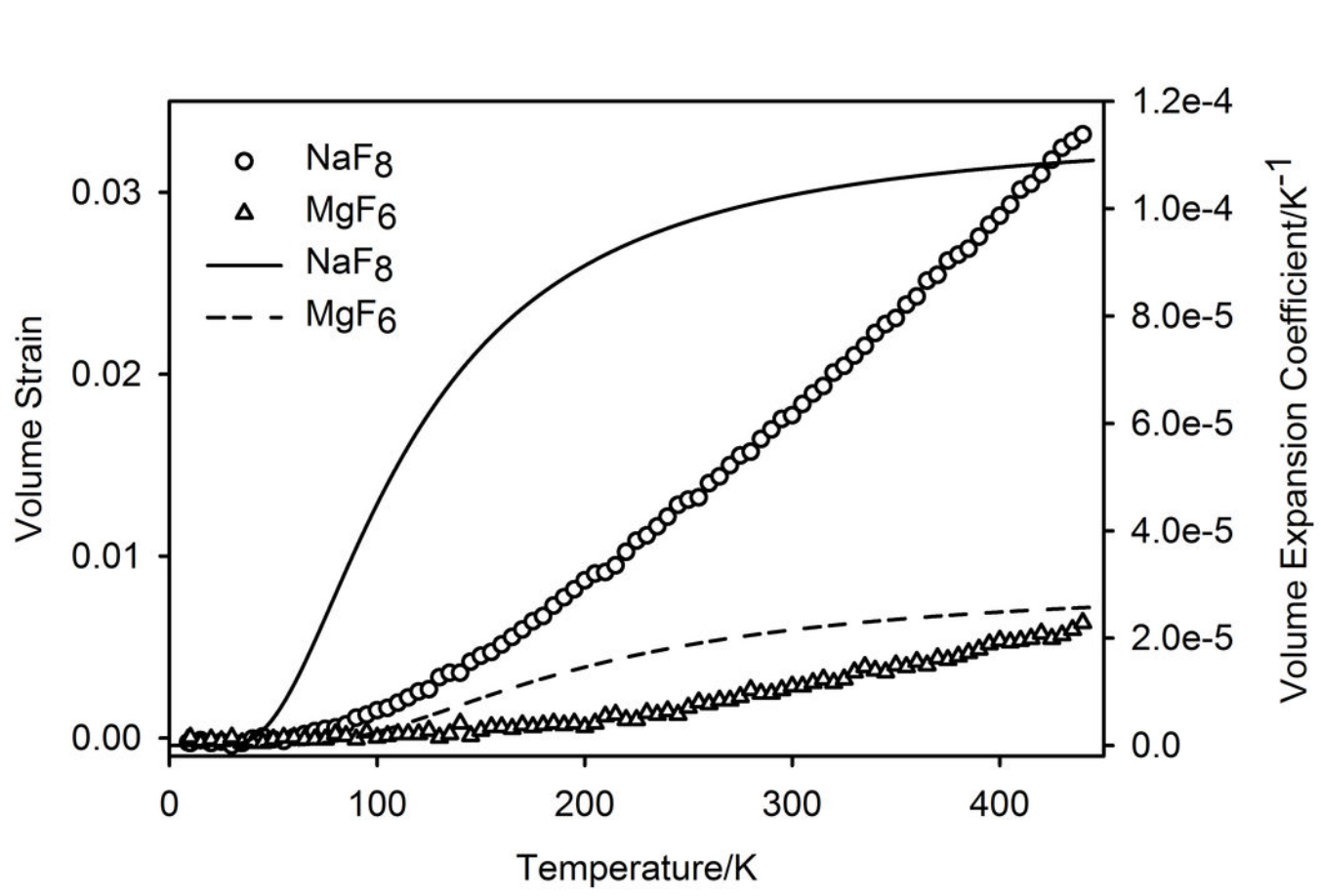
NaF8
MgF6
NaF8
MgF6
Volume Strain
Volume Expansion Coefficient/K-1
Temperature/K
0.00
0.01
0.02
0.03
0
100
200
300
400
0.0
2.0e-5
4.0e-5
6.0e-5
8.0e-5
1.0e-4
1.2e-4

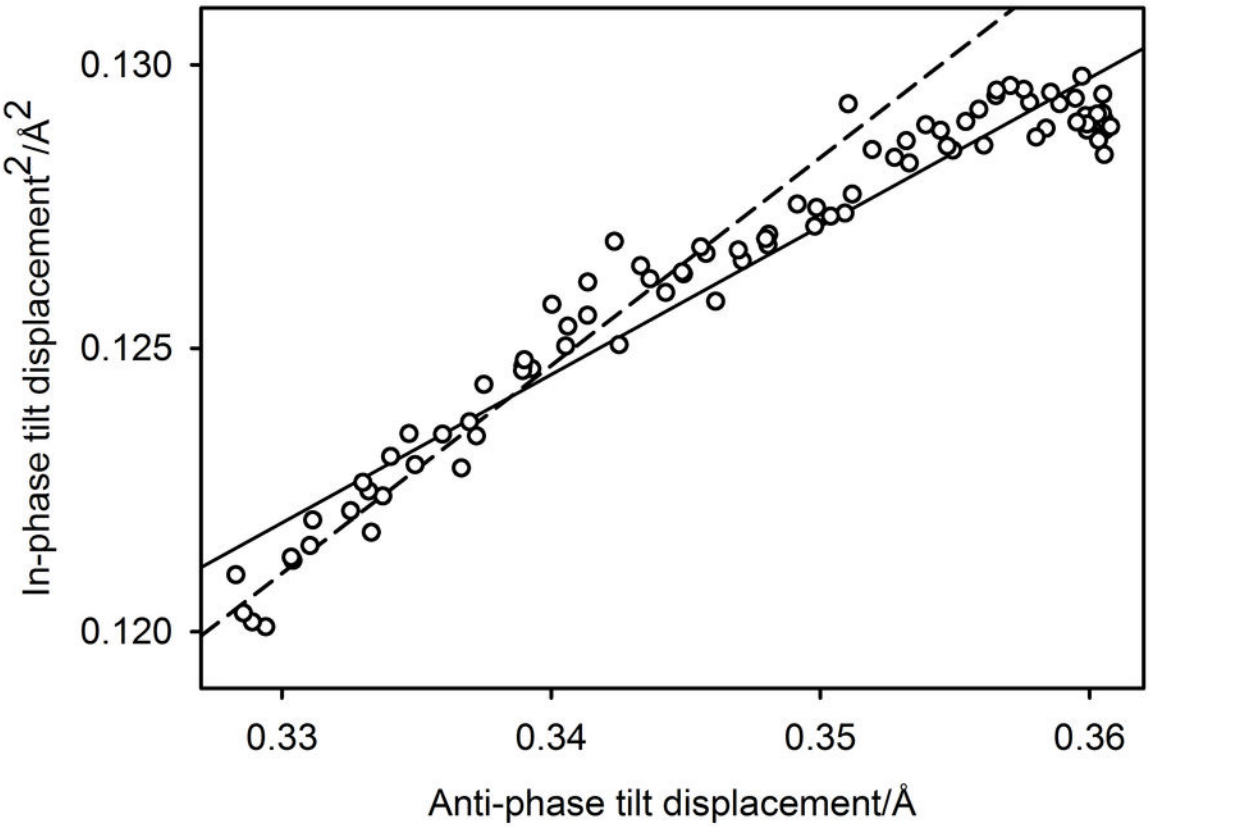
0.130
0.125
0.120
In-phase tilt displacement^2/Å^2
0.33
0.34
0.35
0.36
Anti-phase tilt displacement/Å